communications biology

A Nature Portfolio journal

Article

https://doi.org/10.1038/s42003-026-10032-2

Data-driven mouse motor thalamus model reveals topography and spatial weight scaling govern spindle dynamics

Francesco Jamal Sheiban[1] ✉, Alberto Antonietti[1], Muhammed Furkan Beyazyüz[1], Robin De Schepper[2], Carmen Alonso-Martínez[3], Mario Rubio-Teves[3], Francisco Clascá[3], Egidio D'Angelo[2] & Alessandra Pedrocchi[1]

The thalamus plays a crucial role in motor control but its complex circuitry remains poorly understood. Existing computational models often lack anatomical detail, hindering investigations on how structure influences function. Here we present a data-driven 3D anatomical scaffold model (a geometrically constrained virtual circuit) of mouse motor thalamic nuclei, built by integrating publicly available datasets, anatomical descriptions, geometric constraints and circuit-level findings to reproduce topographical organization and structural boundaries observed experimentally. Network simulations demonstrate sustained spindle oscillations at physiologically realistic frequencies, with propagation velocities matching observations from thalamic slices. Systematic ablation reveals that both topography and distance-dependent synaptic weights are necessary for physiological dynamics, establishing architectural design principles for spatially organized circuits. These findings generalize beyond the motor thalamus: the open-source pipeline provides a reusable framework for data-driven circuit reconstruction, linking anatomical organisation to emergent network dynamics across brain regions.

The conventional perception of the thalamus acting as a simple relay of peripheral sensory information to the cortex has recently been challenged and reconsidered[1]. Current evidence indicates that the thalamus engages in intricate sensorimotor processing through its complex circuitry that serves to gate and otherwise control the flow of information to cortex[2]. Specifically, the functional neuroanatomy of the thalamus suggests that it has a crucial role in at least four partially overlapping canonical functions. It promotes focused cortical activity, facilitates interregional coupling, supports changes in network topology and dimensionality, and enables and modulating temporal neuronal variability[3]. Moreover, direct convergence of different inputs onto the thalamic projection neurons creates computational architectures that vary widely among different thalamic nuclei, and even within the same nucleus[4,5]. On a cognitive level, a recent hypothesis attributes a "blackboard role" to the thalamus. This role is characterized by serving as a central repository of information in which computations from different cortical and subcortical modules are composed, coordinated, and integrated[6,7]. Thus, it is now commonly understood that there exists a profound interconnection between the thalamus and cortex, wherein their functionality is mutually dependent.

Correspondingly, computational models of the thalamus have evolved through three distinct paradigm shifts over the past 30 years, from simple relay implementations to sophisticated multi-scale brain simulations. A first, foundational period established the transition from viewing the thalamus as a passive sensory relay to understanding it as an active oscillatory circuit. This period was pioneered by Destexhe, Sejnowski, and colleagues who introduced biophysically detailed models incorporating T-type calcium channels for spindle waves generation[8,9]. Then, a second paradigm emerged with oscillatory models employing point neurons for larger scale networks[10] and multi-scale models. Notable examples include Izhikevich and Edelman's landmark million-neuron simulation[11] and Hill and Tononi's comprehensive sleep-wake model[12]. Finally, the current state of the art integrates data-driven biological realism, with models like the Blue Brain Project's thalamoreticular circuit incorporating morpho-electrical cell types[13] and contemporary AI-integrated approaches to model cognitive functions[14].

However, existing thalamocortical computational models exhibit significant limitations that constrain their applicability to motor circuit

[1]Department of Electronics, Information and Bioengineering, Politecnico di Milano, Milan, Italy. [2]Department of Brain and Behavioral Sciences, University of Pavia, Pavia, Italy. [3]Department of Anatomy, Histology and Neuroscience, Universidad Autónoma de Madrid, Madrid, Spain.
✉e-mail: francescojamal.sheiban@mail.polimi.it

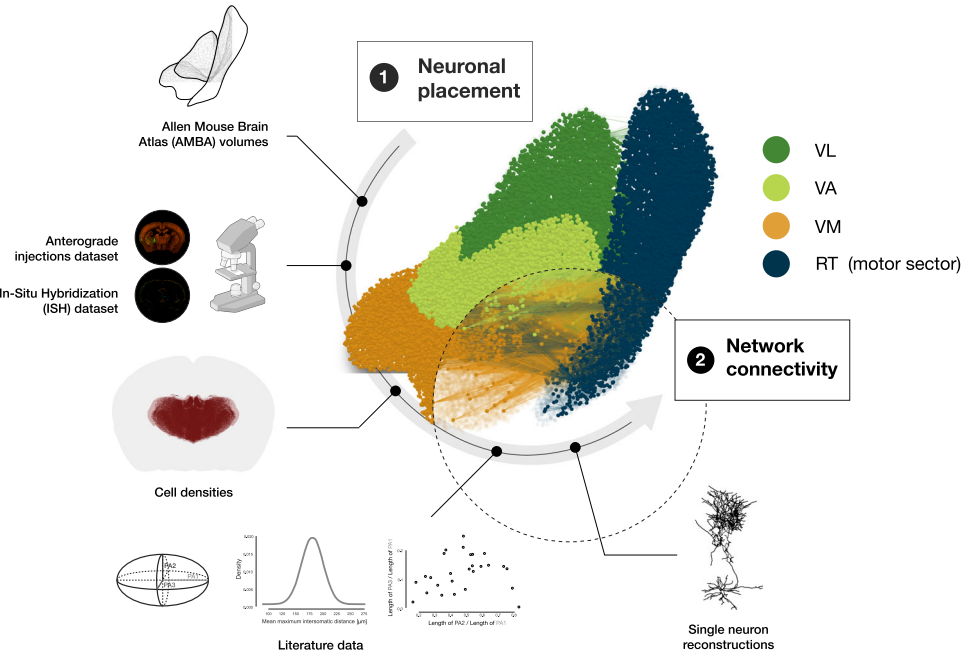

Fig. 1 | Reconstruction pipeline. The reconstruction pipeline followed two steps. The reconstruction pipeline began with the delineations of target nuclei sourced from the Allen Mouse Brain Atlas (AMBA). These AMBA delineations were then enhanced by integrating data from anterograde tracing and in situ hybridization (ISH) studies. Inset image credits: Allen Institute for Brain Science; reproduced from the Allen Mouse Brain Connectivity Atlas (experiment 267929554, image 63 of 140, connectivity.brain-map.org/projection/experiment/267929554)[52,73], and the Allen Mouse Brain Atlas (experiment 71717640, image 48 of 155, mouse.brain-map.org/experiment/show/71717640)[48,74]. This enhancement enabled precise differentiation between ventral anterior (VA) and ventral lateral (VL) nuclei within the ventro-anterolateral complex, and isolation of the reticular nucleus (RT) motor sector from the broader RT volume presented in the AMBA. Neurons were then placed in the identified virtual volumes following the positions reported in the Blue Brain Cell Atlas (VL neurons are shown in dark green, VA neurons in light green, VM neurons in orange, and RT motor sector neurons in dark teal). Finally, connections were formed using a combination of knowledge-based rules and data-driven connectivity rules. The parameters for these rules were derived from literature data and single neuron reconstructions, resulting in a realistic and validated representation of neuronal connectivity. (Note that the figure only shows a fraction of the formed connections for the sake of clarity).

investigation. Large-scale anatomically realistic models, while achieving impressive neuron counts, employ simplified spatial organization, such as layered planes[12] or hexagonal column structures[13] that fail to capture the complex topographical relationships essential for motor thalamic function. Detailed biophysical models focus predominantly on sensory nuclei, particularly somatosensory systems[15,16], leaving motor-specific nuclei largely unexplored.

Comprehensive microscale point-neuron models of the thalamus are scarce, and current models[10,17] lack anatomical specificity fundamental to gain a deeper understanding of the neural mechanisms which are strongly dependent on structural organization[18]. Most critically, no existing computational model explicitly distinguishes between basal ganglia and cerebellar recipient territories within motor thalamic nuclei, despite mounting evidence for their functional segregation[19,20].

Our data-driven anatomical model addresses these fundamental limitations through two key innovations. First, we implement input-based functional parcellation using molecular marker distributions (Calbindin expression) to distinguish basal ganglia- and cerebellar-recipient territories within motor thalamic nuclei, moving beyond the cytoarchitectonic boundaries used in standard atlases[19]. Second, and most critically, the model's 3D anatomical scaffold encodes calculated inter-neuronal distances, enabling realistic simulation of spatiotemporal phenomena, including distance-dependent synaptic weights and topographic connectivity, that are impossible to capture in existing point-neuron models[10,17]. Together, these features generate emergent spindle oscillations at physiologically realistic frequencies and, through systematic ablation, reveal that both spatial weight scaling and topographic organization are necessary for physiological network dynamics. The pipeline is implemented using the open-source Brain Scaffold Builder (BSB)[21], facilitating replication and extension to other brain regions, and the explicit anatomical distinction between cerebellar and basal ganglia recipient territories provides a foundation for future investigation of their distinct contributions to motor control.

Results

The overall reconstruction pipeline (Fig. 1) proceeded in two sequential stages (namely neuronal placement and network connectivity) implemented using the open-source BSB framework[21]. Target volumes were delineated from the Allen Mouse Brain Common Coordinate Framework (CCF)[22]. Given the bilateral symmetry of thalamic structures[23], a single hemisphere was modeled to reduce computational demand.

The modeled region comprises three nuclear groups with distinct functional roles in motor thalamocortical circuits (described in detail in "Methods"): the ventral anterior-lateral (VAL) complex, which was further subdivided into a ventral anterior (VA) territory receiving basal ganglia inputs and a ventral lateral (VL) territory receiving cerebellar inputs based on differential Calbindin1 (*Calb1*) expression[19,20]; the ventromedial (VM) nucleus, targeted by substantia nigra reticulata projections[20]; and the motor sector of the reticular (RT) nucleus, which maintains reciprocal inhibitory connections with VAL and VM[24,25]. Neurons were positioned following cell coordinates from the Blue Brain Project (BBP) Mouse Cell Atlas[26], yielding a scaffold of 56,321 neurons across the four partitions (Table 1).

The network was wired through three anatomically informed connectivity strategies, each following a common logic: spatial filtering first identified synaptic candidates based on cell coordinates, then connections were assigned within the candidate set according to divergence ratios reflecting literature data (see "Methods" for the full specification of each strategy). For thalamocortical-to-reticular (TC → RT) projections, a topographic vector field mapped each VAL-VM voxel to a corresponding position in RT, and synaptic candidates were selected within a cylindrical search volume around each cell's projected branching point (Fig. 2). For intra-reticular (RT → RT) connections, an ellipsoidal mask captured the anisotropic geometry of experimentally characterized dendritic clusters[27], incorporating both chemical GABAergic synapses and gap junctions (Fig. 3). For reticular-to-thalamocortical (RT → TC) projections, the vector field was inverted and synthetic axonal arbors were grown within confined

subvolumes using a space colonization algorithm[28], guided by templates derived from individually reconstructed reticular cells[29] (Fig. 4).

To assess the functional implications of the reconstructed architecture, we simulated the full-scale scaffold using the Neural Simulation Tool (NEST) with individual thalamocortical (TC) and reticular (RT) neurons modeled as Adaptive Exponential Integrate-and-Fire (AdEx) neurons[30], parameterized with cell-type-specific adaptation values reproducing relay-cell and pacemaker firing modes (see "Methods" and Table S3 for complete specifications). Synaptic weights and conduction delays were scaled with inter-somatic Euclidean distance, embedding the scaffold's physical dimensions into the network dynamics. To dissect which architectural features drive emergent activity, the intact model was compared against two ablation conditions: one removing distance-dependent synaptic weights while preserving topography (testing the role of spatial scale in preventing runaway synchronization), and one shuffling the anatomical connectivity while preserving degree distributions and distance-dependent rules (testing the role of topographic organization in supporting coherent wave propagation).

Table 1 | Network dimensions

Partition	Volume [mm^3]	Number of neurons	Neuron type	Density [μm^{-3}]
VA	0.185	11659	Exc.	6.317×10^{-5}
VL	0.224	12471	Exc.	5.575×10^{-5}
VM	0.463	17890	Exc.	3.865×10^{-5}
RT	0.271	14301	Inh.	5.270×10^{-5}
Total:	1.143	56321		

Bold type indicates column headers.
The volumes, densities, and number and type of cells for each partition.

Neuronal placement

We validated our VA-VL delineation by comparing it with the findings reported in another Alonso-Martínez et al.[20], which specifically characterized subcortical inputs to the motor thalamus. Existing knowledge indicates that the VM and VA nuclei predominantly receive inputs from the basal ganglia, whereas the VL nucleus is the primary recipient of cerebellar axons[19,20]. Thus, we registered the coronal slices ($n = 9$ slices) illustrations representing basal ganglia and cerebellar thalamic targets reported in the paper to the Allen CCF[22] and compared the VA and VL regions. As seen in Fig. S6, the delineations are analogous, with VA neurons occupying a thin layer of the ventral VAL nucleus. It is worth noting that a direct one-to-one correspondence was not expected, due to variations arising from the use of different sources of data and reference atlases for identifying the delineations. Nonetheless, the proposed subdivision matches what is known from literature, and will enable to simulate specific cerebellar or basal inputs during simulations.

The RT segmentation already matched the expected rostral position[31], and we further validated our approach with two sets of data. We first used the Allen Mouse Brain Connectivity Atlas tracing experiments to both validate the scalar field mapping of thalamocortical positions onto RT, and to assess that the projection density voxels of experiments with injection source in the ventral posteromedial nucleus (VPM) would not be included in the segmentation. This exclusion was necessary because VPM crosses to the somatosensory sector of RT. To ensure robust validation, we selected experiments with high injection target specificity, confirmed through detailed examination of tracer distribution at the injection sites (Fig. S3). Further, we verified that individual RT cells from Hádinger et al.[29] that were manually traced and observed to project back to either VAL or VM would all belong to the motor delineation we identified. As can be seen in Fig. S7, the volumetric mask obtained contains all the motor-related somas. The mask is not intersected by somatosensory axons, and the spatial topography is preserved when mapping the VAL and VM voxels using the vector fields.

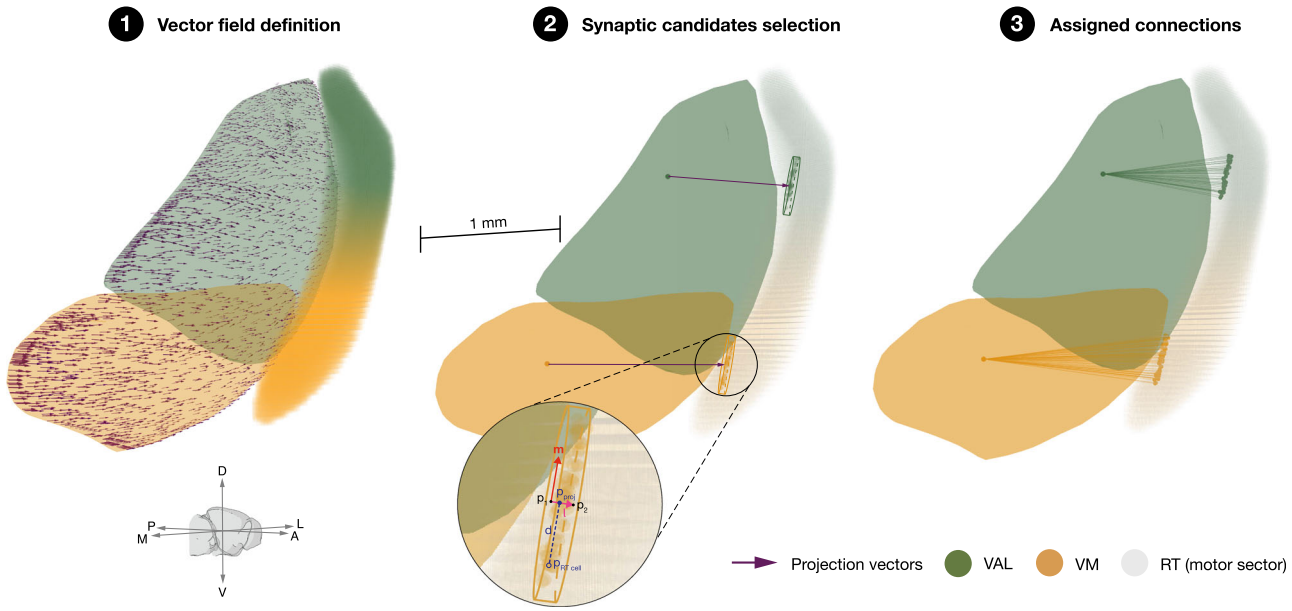

Fig. 2 | Thalamo-reticular connection strategy. Thalamocortical cells are connected to the motor sector of the reticular nucleus following geometrical constraints. First, each voxel of the VAL-VM volume was mapped to a specific point within the motor RT using a vector field, preserving a topographical relation. Panel 1 shows the vector field together with the projected position of each VAL-VM voxel in RT, forming a topographical gradient. Projection vectors are shown as purple arrows; VAL volume in dark green, VM in orange, RT motor sector in gray. Two random thalamocortical cells are shown to further illustrate the connection strategy: first, synaptic candidates were selected using a cylindrical search space centered on a point determined by translating the thalamocortical cell soma according to its associated field vector (Panel 2). The cylinder had radius $r \in \mathcal{N}(100, 90^2)$ and height $h = 20\ \mu$m. Using Plücker coordinates, the synaptic candidates were identified based on their distance (d) to the cylinder axis, $\mathbf{l}$, and the projection of their position onto the axis, $\mathbf{p}_{\text{proj}}$. Reticular cells whose distance d was lower than the radius and whose projection fell between $\mathbf{p}_1$ and $\mathbf{p}_2$, were selected as synaptic candidates, being geometrically confined within the search space. Finally, a number of cells is randomly selected among the synaptic candidates to form the connection, according to a beta distribution (Panel 3).

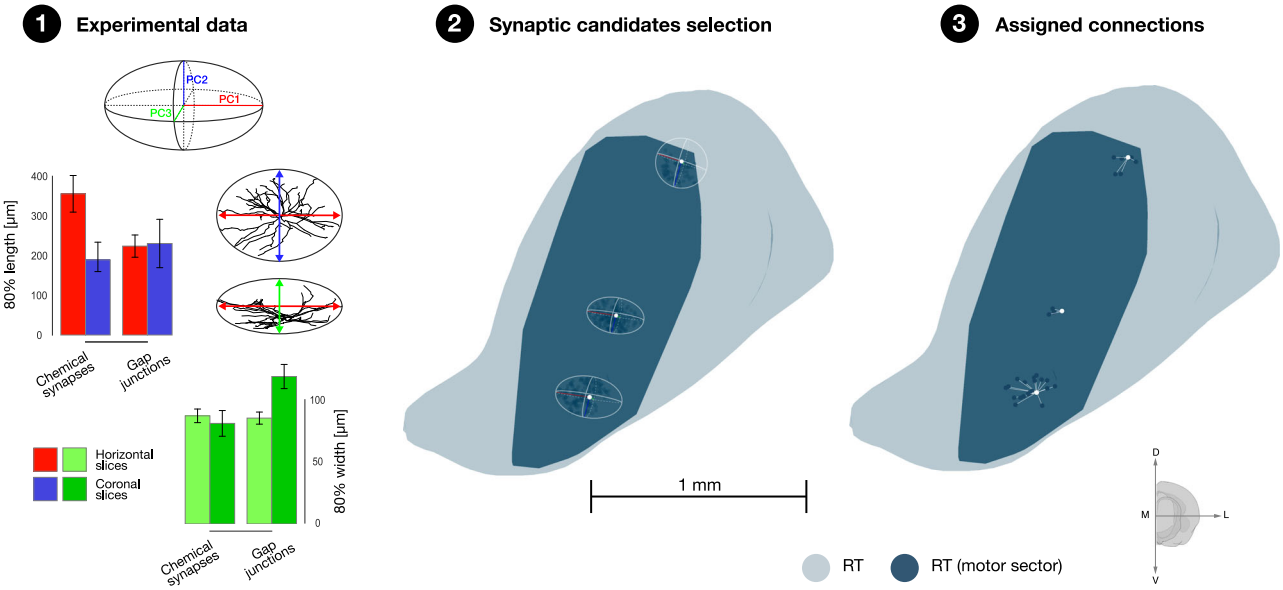

Fig. 3 | Reticulo-reticular connection strategy. Reticular cells are interconnected in elongated clusters whose spatial extent has been experimentally characterized (Panel 1). An ellipsoidal model was used to capture the anisotropic geometry of these clusters, with semi-axes aligned to the first (PC1, red), second (PC2, blue), and third (PC3, green) principal components of the dendritic volumetric spread. The dendritic morphology of a representative reticular neuron (reconstruction AA0399, MouseLight project[70]) is shown in two slice orientations used in the reference study: coronal (blue and red arrows indicating the 80% length and width measurement axes, respectively) and horizontal (green and red arrows). Bar plots display the 80% length of chemical synaptic and gap junction connectivity footprints measured in horizontal (red bars) and coronal (blue bars) slices, and the 80% width measured in horizontal (light green bars) and coronal (dark green bars) slices. Error bars represent mean ± standard error of the mean (SEM) ($n = 6$ slices per orientation). Individual data points are not shown as raw values were unavailable from the original publication, with means ± SEM extracted via digital tracing from published figures in Deleuze and Huguenard[27] using curve-digitization software. Reticulo-reticular connections were formed using ellipsoidal regions for synaptic candidate selection (Panel 2). Each ellipsoid was parameterized with semi-axes lengths drawn from the experimental distributions shown in Panel 1, and was centered and oriented around each reticular cell according to the principal components. White ellipses indicate candidate selection volumes around three example reticular cells (white dots); dark teal dots represent candidate postsynaptic neurons. Each cell was then randomly connected to a subset of candidates, with the number of connections sampled from a beta distribution (Panel 3). Dark lines indicate assigned connections. Light gray volume: reticular nucleus (RT); dark teal volume: RT motor sector. Scale bar: 1 mm. Anatomical axes: D, dorsal; V, ventral; M, medial; L, lateral.

Network connectivity

To validate the network connectivity reconstructed through the proposed connection strategies, we compared our model to existing studies. For clarity, we will refer to our model as the "scaffold model". We compared it to the most detailed in silico thalamic study available[13] and to functional studies investigating the synaptic connectivity between thalamic nuclei and the thalamic reticular nucleus[32,33].

We compared the degree distributions of the generated scaffold network against the reference biological model (Fig. 5). The degree of a neuron is defined as the number of synaptic targets a neuron projects to (out-degree) or receives from (in-degree). The out-degree distribution of the scaffold model is constrained by the number of connections assigned among synaptic candidates in the connection strategies. This distribution follows a beta distribution which has been tuned on values known from literature (as described in the "Materials and Methods" section). This results in distributions that largely approximate the reference data[13], yet reveal specific topological differences with functional implications.

The scaffold model exhibits a higher mean out-degree than the reference, suggesting that individual reticular cells in the scaffold model exert a broader inhibitory influence, projecting to a larger number of thalamocortical neurons. Conversely, the corresponding in-degree distribution is skewed leftward with a peak near zero but possesses a significant heavy tail. This topology implies a sparse but heavy connectivity, in which the average thalamocortical cell receives fewer reticular inputs than in the reference model, but a subset of thalamic cells is heavily inhibited. This structure preserves the capacity for strong reticular inhibition despite lower average convergence, potentially facilitating competitive "winner-take-all" dynamics where specific thalamic streams are strongly suppressed while others are disinhibited[34]. Thalamoreticular in-degree distributions in the scaffold model are notably broader than the sharper peaks observed in Iavarone et al.[13], indicating that reticular neurons in the scaffold model integrate excitatory inputs from a more variable number of thalamocortical cells. Rather than a uniform mapping, this heterogeneity suggests that RT operates as a diverse integrator, where some "hub" reticular cells monitor widespread thalamic activity while others process more localized streams. Finally, reticuloreticular connectivity shows increased variance for both types of connections. The degree distributions are flatter and broader in the scaffold model. Reticuloreticular chemical connections in the scaffold model show a right-shifted out-degree peak, suggesting a stronger internal inhibitory drive within RT itself. This increased interconnectivity and structural variability could enhance the synchronizing capabilities of RT, a key feature in generating sleep spindles and regulating thalamocortical oscillations[35].

After comparing the degree distributions, we sought to replicate the results found in functional studies investigating the organization of the thalamoreticular and reticulothalamic pathways, respectively[32,33], to examine the topographical structure of the scaffold model. We sliced the virtual volume with a plane oriented as reported in the studies, and sampled the synaptic connections found in 200 µm thick slices, both from thalamocortical cells to reticular cells and viceversa. As can be seen in Fig. 6, the topographical organization of the thalamoreticular connections in the scaffold model closely resembles that found in the reference study[32]. Cells closer to the thalamoreticular border project to the reticular outer tier, and cells further from the border project to the inner tier (Pearson correlation coefficient: -0.777, $p < 0.0001$).

Similarly, we plotted the dorsal-ventral and lateral-medial distances of the reticular cells converging to single thalamocortical cells with respect to a reference point. We found significant correlations between the dorsal-ventral (Pearson correlation coefficient: 0.839, $p < 0.0001$) and lateral-medial (Pearson correlation coefficient: 0.842, $p < 0.0001$) coordinates, suggesting topographic organization of these reticulothalamic projections in

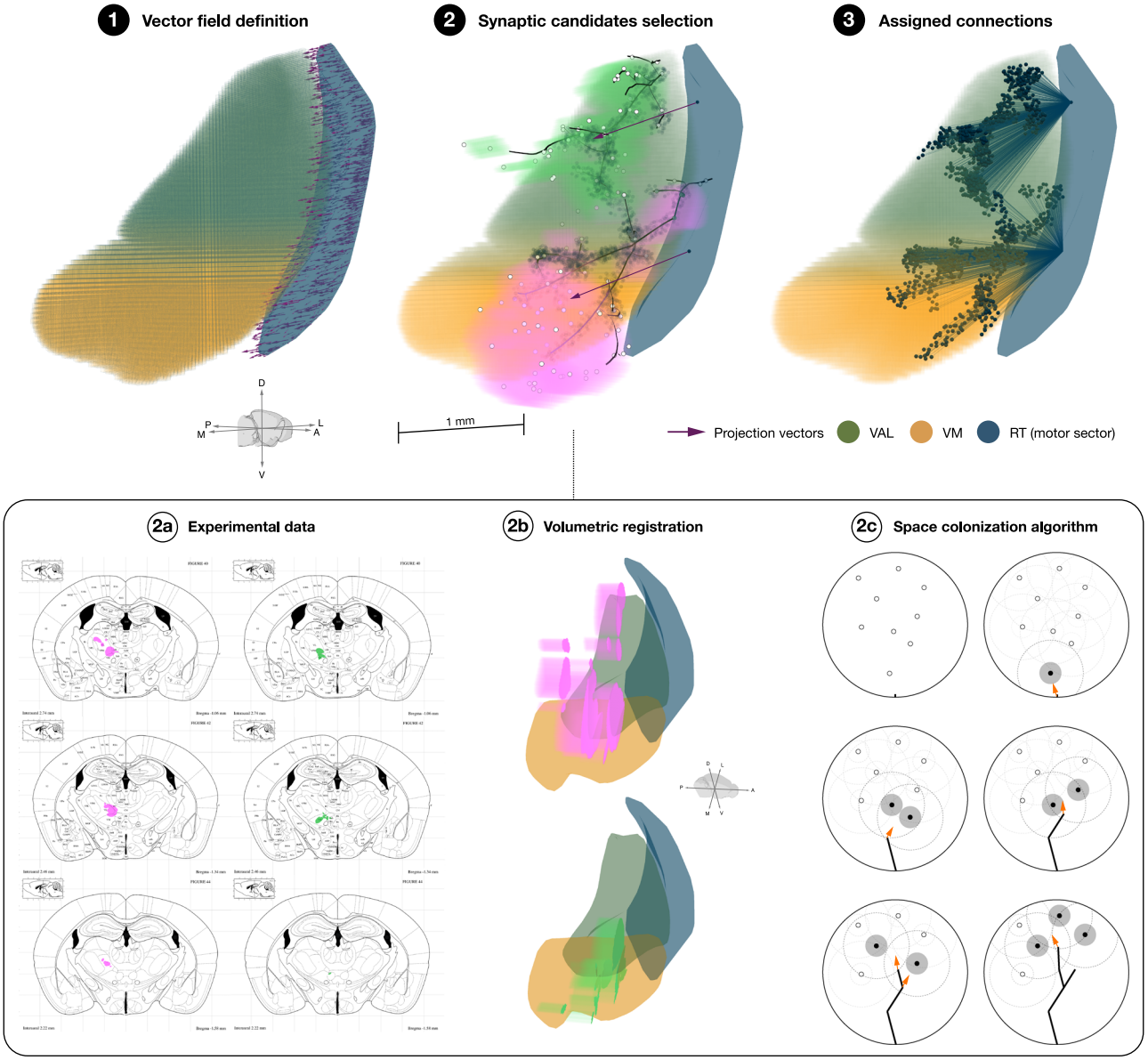

Fig. 4 | Reticulo-thalamic connection strategy. Reticular cells in the motor sector of the reticular nucleus are connected to the thalamocortical cells following both geometrical constraints and algorithmically augmented data. First, each voxel of motor RT was mapped to a corresponding voxel of the VAL-VM volume using a vector field, akin to the thalamoreticular strategy (Panel 1). Synaptic candidates were chosen as a result of an algorithmic data augmentation process (Panel 2). Specifically, the authors of[29] kindly shared atlas maps of 11 reticular cells projecting to either VAL and VM, showing their soma positions and dendritic and axonal fields (2a). These coronal maps were registered to their corresponding 3D position in the Allen CCF and linearly expanded on the antero-posterior axis, forming volumetric templates in which to grow synthetic axons (2b). The axons were grown using an algorithm known as "space colonization". The algorithm works as follows: first, a volume is filled with leaves (white dots). Each leaf has a surrounding area of influence (outer circle) and a reaching point (inner circle). A tree is grown iteratively by letting the branch terminals grow towards active leaves (orange arrows), i.e. those leaves whose area of influence contains at least one branch terminal. Once a leaf is reached, it cannot further influence the growth process. The algorithm stops once all leaves have been reached or after a fixed number of steps (2c). For each reticular cell, a volumetric template was first positioned according to the vector associated to its field position, and filled with leaves following a Gaussian spatial distribution. Then a synthetic axon was grown within the volume using the space colonization algorithm, and all cells within a fixed distance from the axon were considered as synaptic candidate (Panel 2). Each reticular cell was then connected to its synaptic candidates, with a number of connections proportionally influenced by both the density of boutons and the length of the synthetic axon (Panel 3). Projection vectors are shown as purple arrows; VAL volume in dark green, VM in orange, RT motor sector in dark gray. In panel 2c, white dots represent leaves and orange arrows indicate active growth directions.

the scaffold model (as reported experimentally[33]) (Fig. 7). Together, these finding demonstrate that the connectivity rules adopted in the reconstruction process, albeit simple and based on anatomically-informed geometrical constraints, were able to capture the intricate topographical organization of the thalamoreticular and reticulothalamic connections. Fig. S8 presents representative examples of single-neuron input-output maps, demonstrating the distinct spatial organization and connection patterns that emerge from our anatomically-informed connectivity rules.

Finally, we compared the percentage of disynaptic thalamo-reticulo-thalamic connections forming closed loops in the scaffold model to those found in literature[36] and in Iavarone et al.[13]. As can be seen in Table S1, the scaffold model better approximates the range of closed dysinaptic loops found in literature, even though no explicit constraints were enforced during the process of wiring the connections. We believe that this is due to the scaffold model using volumetric placement that closely follows the anatomical boundaries reported in the Allen CCF[22] as

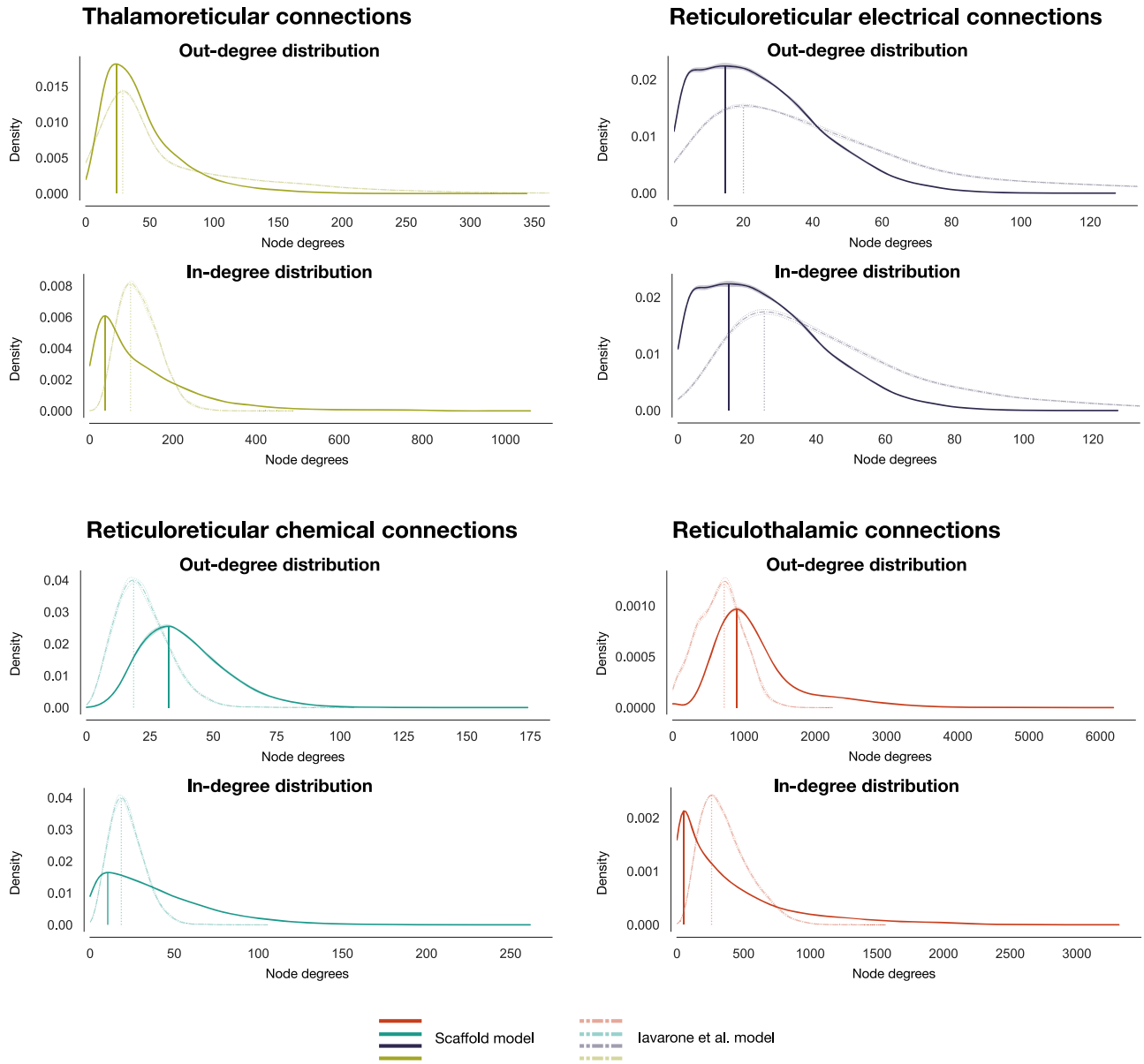

Fig. 5 | Degree distributions. The degree distributions have been plotted as a kernel density estimate (KDE) plot, to normalize the distributions between the two models, given the different amount of cells and synapses. The first and third rows show the out-degree distributions for the four types of connections, while the second and fourth rows show the in-degree ones. The scaffold model distributions are represented by a solid line, while the ones from Iavarone et al.[13] are represented by a dash-dotted line. Vertical lines indicate the peak density values. The scaffold model generally reproduces the distributions of the reference data but exhibits distinct topological features. Notably, reticulothalamic connections in the scaffold model show a right-shifted out-degree peak, indicating higher divergence, while the in-degree distribution is heavily skewed toward lower values with a long tail, suggesting sparse but heterogeneous convergence onto thalamocortical cells. Thalamoreticular in-degree appear broader in the scaffold model, implying a more heterogeneous sampling of thalamic inputs by reticular cells. Reticuloreticular connections (both electrical and chemical) generally display broader distributions in the scaffold model, indicating a higher degree of structural variability compared to the reference. Degree distributions were computed across multiple stochastic model instances to ensure statistical robustness, with sample sizes comprising 210,100 thalamocortical and 71,505 reticular neurons from 5 scaffold model instances, compared to 64,856 thalamocortical and 35,567 reticular neurons from 7 reference model instances (Iavarone et al.[13]).

opposed to simplyfing the spatial extent of the model to a column-like structure[13].

Sensitivity analysis

We conducted extensive sensitivity analysis to probe the robustness of our model's key findings against variations in key parameters and assumptions. As acknowledged throughout this study, several model components rely on literature-derived estimates and geometric constraints due to the lack of quantitative anatomical data for motor thalamic circuits.

To address this limitation and evaluate the stability of our primary validation outcomes, we systematically varied four fundamental parameter sets: the *Calb1* density threshold governing VA/VL parcellation, the geometric constraints defining thalamo-reticular connectivity patterns, the beta distribution parameters controlling connection degree assignments, and the spatial proximity thresholds determining reticulothalamic synaptic candidates.

For each parameter variation, we quantified changes in model performance using the same validation metrics employed in our primary analysis, including comparisons to experimental parcellation data,

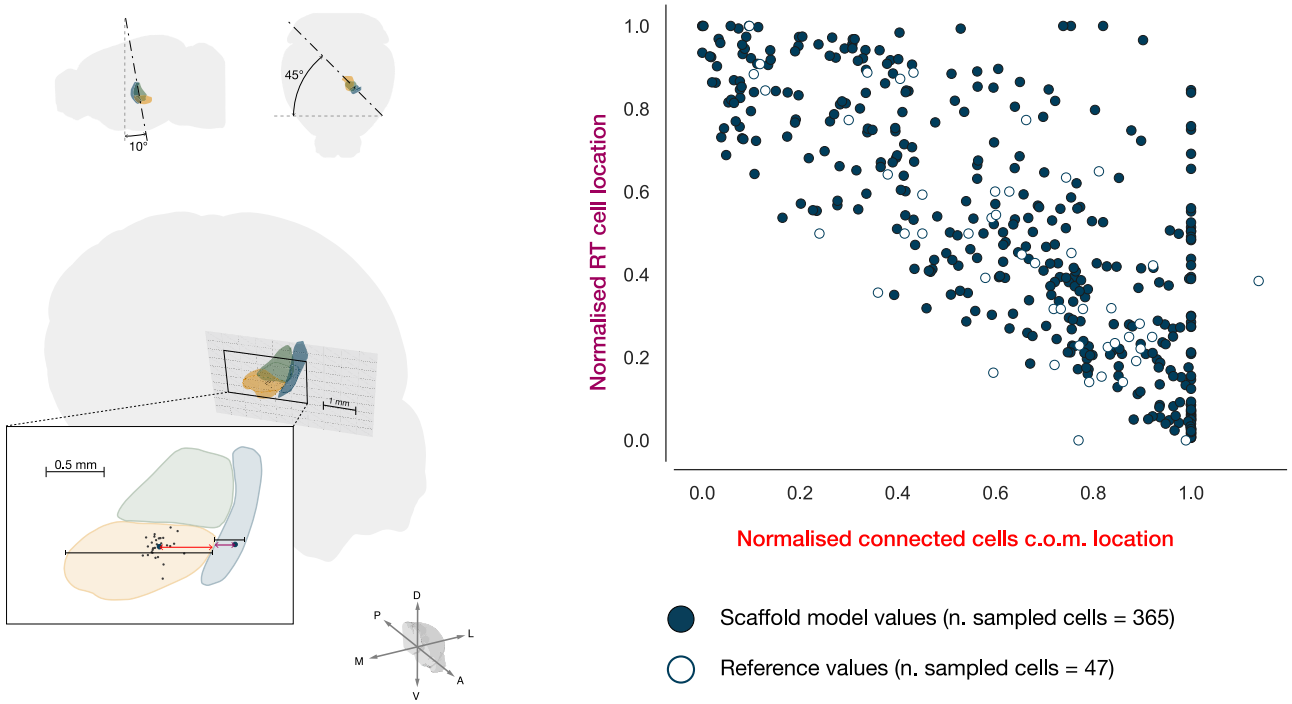

Fig. 6 | Topographic organization of thalamoreticular inputs. The validation has been done using the same slicing plane as in Lam and Sherman,[32], that has been shown to preserve most of the thalamoreticular connectivity on biological samples. It is a plane tilted in the anteroposterior direction by 10° and 45° latero-medially. For each reticular cell that was sampled, the plane was first centered around the cell's soma and then the positions of the connected thalamic lying within 150 μm for each side of the plane were sampled to simulate a 300 µm slice. Then, we measured the distances with respect to the thalamoreticular border of both the center of mass (c.o.m.) of the connected footprint (red arrow) and the reticular cell itself (purple arrow). We normalized the distances using the values of the segments connecting the thalamic and reticular extremities to the thalamoreticular border, passing through the c.o.m. and reticular cell (black lines). Plotting the pair of values for each sampled cell on a scatterplot reveals a topographic organization similar to that found in the reference study. Cells closer to the reticular nucleus project to the outer tier and those further from the border project to inner tiers. Data extracted from ref. 32.

topographic organization measures, and degree distribution characteristics. This comprehensive sensitivity analysis enables us to distinguish robust model features from parameter-dependent artifacts and provides confidence bounds for our key neuroanatomical and connectivity findings.

To evaluate the robustness of the VA/VL *Calb1* density threshold, we conducted systematic sensitivity analysis using the Dice coefficient[37]. The Dice coefficient is a well-established spatial overlap metric widely employed for validating MRI image segmentation quality and anatomical boundary delineation[38]. The Dice coefficient quantifies the spatial overlap between two binary volumes, with values ranging from 0 (no overlap) to 1 (perfect overlap), providing an objective measure of parcellation accuracy relative to reference anatomical data.

We systematically varied the Calbindin density threshold from 0.05 to 1.0 in increments of 0.05 ($n = 20$ threshold values), generating distinct parcellations for comparison with the reference boundaries reported by Alonso-Martínez et al.[20]. The analysis revealed two distinct optimal coefficients. VA regions achieved maximum Dice coefficient (0.683 ± 0.231) at our originally selected threshold of 0.3, while VL regions demonstrated peak alignment (0.655 ± 0.206) at a higher threshold of 0.7 (Fig. S9, left and right panels). However, substantial intra-slice variability is evident across all threshold values, as demonstrated by the large error bars and heterogeneous patterns visible in the accompanying heatmaps (Fig. S9, heatmap panels).

Several methodological considerations must be acknowledged when interpreting these results. The reference dataset represents schematic anatomical illustrations that underwent extensive digital processing, including extraction from published figures[20], digitization, and registration to the Allen CCF coordinate system using computational pipelines[39]. Consequently, this reference cannot be considered ground truth but rather represents a processed interpretation of the original authors' anatomical observations. Furthermore, the two datasets exhibit fundamental heterogeneity in their derivation methods, atlas frameworks, and spatial resolutions, limiting direct quantitative comparison.

Given these limitations and the mathematical derivation of our threshold from the quantitative transcript-per-million (TPM) data reported in Phillips et al.[19], we maintain the original threshold value of 0.3 for both VA and VL delineation. This approach ensures consistency with the molecular expression data underlying our parcellation strategy while acknowledging that alternative thresholds could yield comparable spatial overlap under different validation frameworks.

We next examined the sensitivity of network connectivity patterns to the beta distribution parameters (α, β)[40] governing connection degree assignments across both thalamo-reticular and reticulo-reticular projections. Given the computational constraints of each connectivity type, we employed complementary optimization strategies: manual parameter exploration for thalamo-reticular connections (assigned during scaffold compilation, which requires several hours on supercomputer infrastructure) and Bayesian optimization for reticulo-reticular connections (assigned offline post-compilation).

For thalamo-reticular projections, five parameter combinations spanning a numerically-close range were tested: (1.0, 21), (1.25, 18), (1.5, 18), (2.0, 20), and (2.5, 15), with model performance evaluated using Kolmogorov-Smirnov (KS) distances against reference degree distributions.[13]

The analysis revealed substantial parameter sensitivity, with KS distances varying by up to 127% (i.e., 0.155–0.352 for the out-degree distribution) across tested combinations (Fig. S10). Our initial parameters (1.25, 18) proved suboptimal, achieving only moderate distributional agreement (out-degree KS = 0.259). The optimal combination (2.5, 15) reduced distributional discrepancy by 41% for out-degree distributions and 28% for in-degree distributions, demonstrating significant improvement in

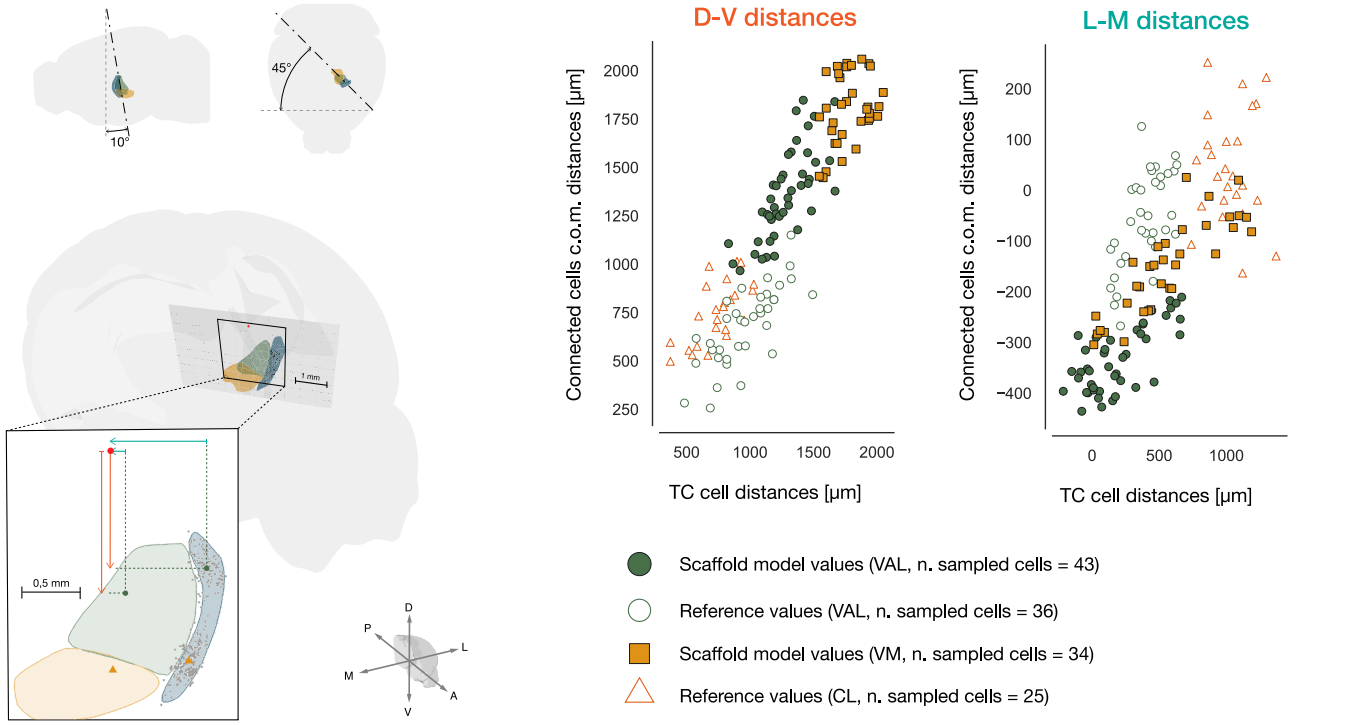

Fig. 7 | Topographic organization of reticulothalamic inputs. Using the same slicing procedure as the one carried out for characterizing thalamoreticular topography, we measured the distances from a fixed reference point, the tip of the hippocampus (as in Lam and Sherman, 2015[33]). For each thalamocortical cell and the center of mass (c.o.m.) of its connected reticular cells, we measured both the dorso-ventral (D-V) distance (red arrows) and the latero-medial (L-M) distance to the reference point, and plotted the resulting pairs in a scatterplot. Similarly as the previous figure, the connections appear to be topographically organized, with a clear pattern emerging from the data. Note that in the original study, the authors sampled the thalamic cells in the ventro-anterior lateral (VAL) and central lateral (CL) nuclei, while we considered cells in the ventro-medial (VM) and VAL nuclei. Since CL is more medial than VAL but roughly at the same height, the reference values show two distinguishable regions in the L-M distances scatterplot. Conversely, as VAL and VM overlap in the L-M axis but are separated in the D-V axis, our value show this separation in the D-V distances plot. Data extracted from[33].

model fidelity. For reticulo-reticular connections, the offline assignment workflow enabled deployment of Gaussian process-based Bayesian optimization across a nine-dimensional parameter space (n, α, β for chemical outdegree, chemical indegree, and gap junction connections). Note that n is a scaling parameter used to increase the range of the beta profile from its original [0,1] domain. Starting from uniform baseline parameters ($\alpha = 1.5, \beta = 22.75$, with varying n), 250 evaluations converged to optimized values that substantially improved agreement with reference data (Fig. S10, middle and bottom rows).

The optimization yielded connection-specific parameters, reducing the combined KS distance from 0.655 to 0.478. Notably, the optimized chemical outdegree distribution achieved a 27% improvement (KS reduction from 0.220 to 0.161), while gap junction distributions showed 62% improvement (KS reduction from 0.435 to 0.167).

These optimized parameters were adopted in the final model for both connection types, demonstrating the framework's capacity for systematic refinement and validation against empirical benchmarks through complementary optimization strategies tailored to computational feasibility constraints.

To assess the robustness of the thalamo-reticular cylindrical synaptic selection strategy, we varied the geometric parameters defining the cylindrical search volumes used to identify synaptic candidates, with parameters originally constrained by anatomical observations of axon collateral morphology. Specifically, cylinder height (h) and radius bounds (r_{min}, r_{max}) were originally set to 20 µm and [90, 190] µm, respectively, based on the bimodal distribution of collateral spatial extent reported by Harris[41].

To assess whether the observed topographic organization (Pearson correlation coefficient, $r = -0.7772$ [95% CI: −0.8149, −0.7331], $p = 4.9268 \times 10^{-75}$, $n = 365$ independent cells) represents a robust emergent property rather than a parameter-dependent artifact, we varied these geometric parameters across five configurations: proportionally smaller ($h = 15$ µm, $r \in [68, 143]$ µm), proportionally larger ($h = 25$ µm, $r \in [113, 238]$ µm), ultra-flat ($h = 10$ µm, $r \in [90, 190]$ µm), and more spherical ($h = 40$ µm, $r \in [90, 190]$ µm) geometries, in addition to the reference configuration.

Topographic correlations remained consistently strong across all parameter sets (r range: −0.7772 to −0.8299), with only 6.8% variation despite spanning a fourfold range in cylinder height and 25% scaling in radial extent (Fig. S11). The proportionally smaller configuration yielded the strongest correlation ($r = -0.8299$ [95% CI: −0.8599, −0.7941], $p = 3.3306 \times 10^{-90}$, $n = 350$ independent cells), suggesting that slightly constrained collateral fields may enhance topographic precision. These findings validate that our connectivity rules capture intrinsic organizational principles of motor thalamic circuits that are stable across biologically plausible parameter ranges.

Complementing this analysis, we examined the sensitivity of reticulo-thalamic synaptic selection by systematically varying the radial distance threshold used to identify thalamocortical synaptic candidates near synthetic reticular axonal arbors. The baseline threshold (43.5 µm) was established as a quarter of the average dendritic length of VAL-VM thalamocortical neurons (174 µm), reflecting anatomical evidence that reticular terminals preferentially contact proximal dendritic compartments[42].

We tested five values spanning a 5-fold range: 21.75, 43.5, 65.3, 87, and 108.75 µm, corresponding to 0.125 × , 0.25 × , 0.375 × , 0.5×, and 0.625× of average dendritic length. Mirroring the robustness observed for thalamo-reticular connectivity, all configurations preserved strong topographic organization with dorsal-ventral correlations ranging from $r = 0.8032$ to 0.8895 and lateral-medial correlations from $r = 0.7580$ to

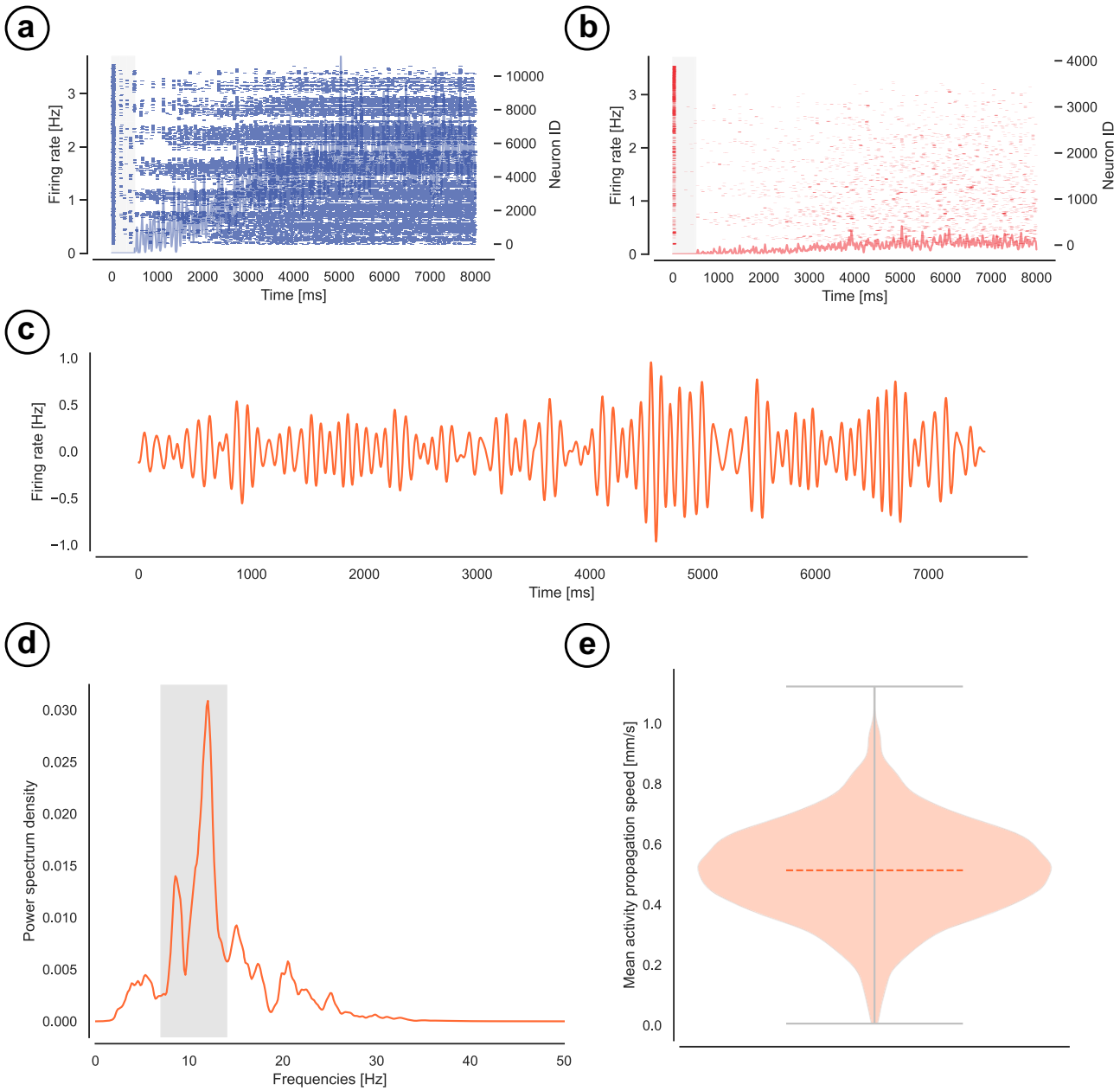

Fig. 8 | Self-sustained spindle oscillations in the full biophysically constrained model. Raw population firing rates with overlaid raster plots showing spike times for RT neurons (**a**) and TC neurons (**b**) over an 8-second simulation following brief, spatially distributed stimulation (20% of TC population, 25 ms duration). RT activity is shown in blue, TC activity in red. **c** Spindle-band filtered population activity (7–14 Hz bandpass) of RT neurons demonstrating sustained rhythmic dynamics with characteristic waxing-and-waning amplitude modulation typical of thalamic spindle oscillations. Gray shaded region (0–500 ms) indicates transient period excluded from steady-state analysis. **d** Power spectral density of high-pass filtered (cut-off frequency 2.5 Hz) RT population activity showing dominant peak around 11–12 Hz within the canonical spindle band (7–14 Hz, gray shaded region), with concentrated spectral power and minimal harmonic content. **e** Violin plot displaying distribution of instantaneous wavefront propagation speeds extracted from spatiotemporal activity analysis. The central dashed line indicates median velocity.

0.8651, representing only 10.8% and 14.1% coefficient variation across the parameter range (full per-configuration statistics reported in Fig. S12).

The most restrictive threshold (21.75 μm) showed slightly reduced lateral-medial organization ($r = 0.758$), potentially reflecting under-sampling of dendritic arbors, while intermediate to larger values (65.3–108.75 μm) maintained consistently strong correlations. The stability of topographic organization across this wide parameter range reinforces the conclusion that spatial patterning in both feedforward and feedback pathways emerges from fundamental geometric principles (e.g., the vector field mapping and space colonization algorithm) rather than from precise parameter tuning, validating the robustness of the reciprocal thalamoreticular circuit organization.

Network simulations

Having established the anatomical accuracy of the reconstructed scaffold, we then investigated whether its spatial organization was sufficient to generate physiologically realistic network dynamics.

Following brief, spatially distributed stimulation, the network rapidly transitioned to a stable, self-sustained oscillatory regime around 11–12 Hz (Fig. 8), matching the canonical frequency of thalamic spindle oscillations observed in vivo and in vitro. The oscillations

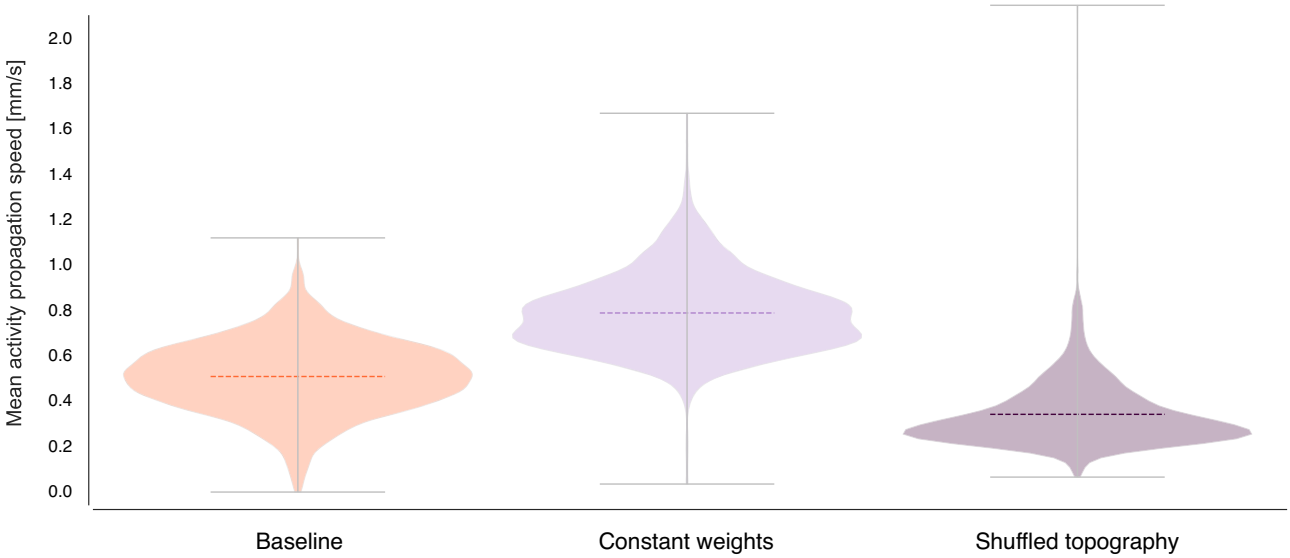

Fig. 9 | Distinct dynamical regimes following ablation of spatial connectivity features. Violin plots showing distributions of instantaneous wavefront propagation speeds across three experimental conditions. (Baseline condition) The baseline model incorporating distance-dependent synaptic weights, distance-dependent conduction delays, and anatomically realistic topography, exhibits controlled phase-coherent wave propagation with median velocity of 0.5 mm s^{-1} (0.3–0.7 mm s^{-1}). (Constant weights condition) Removal of distance-dependent weights while preserving anatomical topography, produces a hypersynchronous regime characterized by accelerated propagation (median 0.8 mm s^{-1}, +60% relative to baseline) with markedly broadened velocity distribution extending to 1.6 mm s^{-1}, reflecting broader recruitment of large neuronal populations. (Shuffled topography condition) Disruption of anatomical connectivity organization through rewiring while maintaining distance-dependent connectivity parameters results in a spatially incoherent regime with suppressed propagation (median 0.30 mm s^{-1}, −40% relative to baseline) and narrow distribution, demonstrating that topographic organization is essential for controlled wave dynamics. Horizontal dashed lines indicate median speed. Baseline condition is represented in orange, constant weights condition in lilac, and shuffled topography condition in purple.

exhibited strong phase-locking between TC and RT populations (phase-locking value, PLV = 0.853), with TC neurons consistently leading RT activity by approximately 10°. Wavefront analysis revealed saltatory propagation dynamics, with instantaneous velocities fluctuating around a median of 0.5 mm s^{-1} (inter-quartile range: 0.3–0.7 mm s^{-1}), quantitatively consistent with measurements from ferret thalamic slices (0.28–1.21 mm s^{-1})[43].

To determine which architectural features were necessary for these dynamics, we compared the full model against the two ablation conditions described in the "Material and Methods" section (Fig. 9).

The intact scaffold maintained controlled, phase-coherent wave propagation. In contrast, removing distance-dependent weights produced a notably different regime characterized by tripled oscillation amplitude and larger recruitment, with propagation velocity accelerating to 0.8 mm s^{-1} (+60 % relative to baseline). This pathological state can be compared to epileptiform discharges, and demonstrates that physical scale and the resulting spatial attenuation are essential constraints preventing runaway synchronization.

Conversely, disrupting the anatomical topography while preserving connectivity statistics suppressed propagation to 0.30 mm s^{-1} (−40% relative to baseline), producing spatially fragmented activity despite intact delays and synaptic weights.

Together, these results establish that the scaffold's three-dimensional organization constitutes a fundamental computational constraint: topographic connectivity patterns support organized wave propagation, while realistic transmission weights prevent pathological recruitment.

Discussion

This study presents a modular bottom-up approach for constructing a detailed thalamoreticular scaffold model, leveraging open-source tools and integrating data from diverse sources (including public datasets, anatomical descriptions, geometric constraints and circuit-level findings).

The resulting anatomical reconstruction accurately replicates the topographical organization and structural boundaries of the motor-related nuclei in the mouse thalamus. While acknowledging the inherent limitations of the model arising from data scarcity and the necessity of employing assumptions based on existing literature, the modularity of our pipeline allows for continuous refinement as circuit-level studies emerge.

The validation process was limited by the lack of quantitative experimental data specifically focusing on the thalamic nuclei included in this model. Fine-grained details, such as the degree distributions of the different types of connections, could only be compared to existing in silico models[13] that are not guaranteed to be accurate, nor refer to motor-related nuclei. Nevertheless, the model has been shown to preserve salient anatomical delineations and a rich topographic organization, that closely mimics what is known from thalamo-reticular anatomical studies.

Thus, this scaffold model improves upon simplified point-neuron thalamoreticular models, to the best of our knowledge, due to its enriched anatomical detail and the utility of this high-resolution spatial modeling is directly demonstrated by functional simulations. The network spontaneously generated stable 11 Hz spindle oscillations with saltatory wave propagation at 0.5 mm s^{-1}, quantitatively matching experimental measurements from thalamic slices[43], without parameter tuning for network behavior. This emergent realism validates the data-driven reconstruction approach and establishes the scaffold as a mechanistic bridge between anatomical structure and network computation.

Systematic ablation of spatial features revealed two fundamental architectural principles. First, physical scale functions as an intrinsic spatial filter: removing distance-dependent weights produced explosive hypersynchronous recruitment with accelerated propagation (0.8 mm s^{-1}), demonstrating that thalamic dimensions prevent pathological synchronization. This mechanism provides a testable framework for understanding disorders where spatiotemporal coordination breaks down, such as absence epilepsy. The model predicts that manipulations selectively affecting the spatial scaling of synaptic weights, rather than their global magnitude, should shift networks between phase-coherent and hypersynchronous regimes. Second, anatomical topography determines organized propagation: disrupting spatial organization while

preserving connectivity statistics suppressed wave velocity to 0.3 mm s^{-1} and produced spatially fragmented dynamics.

Thus, our approach allows investigation of spindle wave propagation and thalamic neuronal dynamics with point neuron networks, instead of resorting to more complex compartmental models[44]. Furthermore, the explicit distinction between VA and VL subnuclei within our model enables investigation of their distinct contributions to the thalamo-cortical motor loop in multi-area simulations[45]. This allows the differentiation of the basal ganglia and cerebellar inputs to the single thalamocortical neurons. Future extensions could incorporate cortical feedback, neuromodulatory control, and behavioral correlates. Such additions would enable to investigate how motor thalamic architecture supports action selection, motor learning, and the integration of subcortical motor commands. The open-source implementation facilitates replication and extension to other thalamic nuclei. It provides a generalizable methodology for data-driven circuit reconstruction that balances anatomical realism with computational tractability.

In conclusion, the proposed thalamic scaffold model provides a valuable platform for future research, facilitating both quantitative validation against emerging experimental data and exploration of intricate neural mechanisms underlying motor control and other thalamic functions. Its modular design allows for continuous refinement as circuit-level studies emerge, ultimately contributing to a more comprehensive understanding of the complex interplay between structure and function in these thalamic nuclei.

Methods

The reconstruction pipeline and modeled nuclei are summarized in "Results"; here, we detail the computational procedures. The workflow is divided into neuronal placement (volume delineation and cell positioning) and network connectivity (three pathway-specific wiring strategies), followed by network simulation and analysis.

Neuronal placement

To accurately position cells within the scaffold, multiple data sources have been collected and integrated. We started outlining the volume to fill using the mesh models provided in the Allen Mouse Brain CCF[22], combining the delineations reported for the target nuclei. Since the thalamus is a bilaterally symmetrical structure[23], we only modeled one hemisphere (namely, the left hemisphere) as to reduce the computational cost required for both building and simulating the model (Fig. S1).

The motor thalamic nuclei modeled in this study exhibit distinct anatomical and molecular characteristics that define their functional roles within thalamocortical circuits.

The VAL complex comprises two functionally distinct subdivisions differentiated by their input patterns and molecular markers[20]. The VA subdivision represents a small dorsal and anterior zone that specifically receives entopeduncular nucleus projections, the rodent equivalent to the primate medial pallidum[20]. VA neurons are characterized by strong Calbindin 28k immunolabeling in neuronal somata, distinguishing them from surrounding regions[20]. This subdivision represents the primary basal ganglia-recipient territory within the motor thalamus. It receives driver-type connections from globus pallidus internus (GPi) inputs characterized by large GABAergic boutons ($> 2\,\mu m^2$ cross-sectional area), and demonstrates convergence patterns where 23.8% of neurons receiving motor cortex layer 5 inputs also receive GPi projections[4]. The VL subdivision is delineated by the presence of large *Slc17a6 (Vglut2+)* cerebellar terminals and the absence of Calbindin 28k somata or nigral/entopeduncular inputs[20]. VL receives the largest glutamatergic terminals from deep cerebellar nuclei with extensive clustering patterns and exhibits driver characteristics, including paired-pulse depression[4].

The VM nucleus is functionally defined as the thalamic zone targeted by substantia nigra reticulata-recipient axons, with constituent cells expressing Calbindin+ immunolabeling[20]. VM is clearly demarcated from the VPM by fibers of the medial lemniscus and demonstrates sophisticated input integration with strong basal ganglia dominance complemented by cerebellar and cortical systems[20]. As defined in recent anatomical studies, VM excludes the most caudolateral part of the cytoarchitectonically-defined VM described in standard atlases, as this caudolateral zone lacks Calbindin expression and nigral inputs while receiving spinothalamic inputs instead[20]. VM neurons exhibit distinctive cortical projection patterns with dense layer 1 terminations creating "matrix-type" connectivity and demonstrate preferential targeting of layer 5B pyramidal tract neurons over layer 6 corticothalamic neurons[4].

The RT nucleus forms a thin inhibitory shell surrounding the dorsal and lateral aspects of the thalamus and is organized into distinct functional sectors corresponding to different sensory and motor modalities[24,25]. RT exhibits sophisticated molecular organization characterized by transcriptomic gradients containing hundreds of genes, with cellular heterogeneity, where neurons at gradient extremes express mutually exclusive markers (*Spp1+* and *Ecel1+*) that correlate with functional properties[31]. The nucleus demonstrates dual intrinsic connectivity through both electrical synapses via gap junctions and chemical GABAergic synapses, enabling synchronization of burst firing while providing lateral inhibition mechanisms[27,46]. RT neurons maintain topographic reciprocal connections with their respective thalamic targets, with individual neurons providing targeted inhibitory control over multiple relay cells while preserving functional segregation of different modality representations[24,47]. For this study, we focused on the rostral RT region that maintains reciprocal connections with VAL and VM nuclei, corresponding to the motor-related sector of the reticular complex.

In the CCF, VA and VL subdivisions are considered as a single area. However, recent findings highlight important distinctions between VA and VL in the mouse thalamus akin to what is also observed in humans and primates. Thus, we integrated in situ hybridisation (ISH) data from the Allen Mouse Brain Atlas[48] to distinguish the two subvolumes based on the Calbindin 1 (*Calb1*) density, since VA neurons predominantly express such gene[19]. We collected the relevant experimental data from the Allen dataset (*Calb1* experiments with coronal orientation, ID: 71717640, 79556672), computed the average values, upscaled the data to match the CCF resolution and then classified the two subvolumes, namely VA and VL, through thresholding.

Specifically, we downloaded the 200 µm per voxel densities from the Allen portal, and used a grid interpolator to upscale the densities to a resolution of 25 µm per voxel. The data was upscaled using the Piecewise Cubic Hermite Interpolating Polynomial (PCHIP)[49], as this method performs better than linear or cubic approximation on real-world data[50,51]. Volumetric data were classified using a binary threshold approach based on normalized *Calb1* density. The threshold value of 0.3 was determined from the differential *Calb1* expression patterns across brain regions reported in the Supplementary Fig. 2 of Phillips et al.[19]. Values were digitally extracted by analyzing pixel distances relative to axis units, and the threshold was calculated as the midpoint between the minimum VA and maximum VL transcript per million (TPM) values, subsequently normalized to the highest expression sample. Voxels exceeding this threshold were classified as VA, distinguishing high-*Calb1* (VA) from low-*Calb1* (VL) regions. The upscaling and thresholding procedure is shown in Fig. S2.

Since it is well-known that the RT is divided into sectors in a highly topographical manner (and that the motor sector is in the anterior part of the RT[24,25]), we segmented the relevant motor sector from the original RT nucleus volume. As RT loci are reciprocally connected with their thalamic targets[24], we used the injection data from the Allen Mouse Brain Connectivity Atlas[52] to identify the volumetric delineation of the motor sector. We queried experiments with the injection source in the VAL and VM nuclei and stored the intersection of the reported thalamocortical projection tracts with the RT volume. And, conversely, we identified the experiments with the injection source in RT whose labeled axons targeted VAL and VM, and stored the voxels from which the axons originated. All injection sites were validated to ensure high target specificity and minimal spillover into adjacent regions (see Fig. S3). By combining the two voxel sets and extracting their convex hull, we obtained a volumetric mask of the desired sector. Since the injection data is sparsely noisy, prior

to combining the volumes, we filtered the dataset according to its local density (as shown in Fig. S4).

Once the volumetric delineations were completed, we placed the neurons in the scaffold according to the cellular positions reported in the BBP Mouse Cell Atlas[26]. To overcome the volumetric differences in the Allen CCF versions used (the Mouse Cell Atlas uses version 2.5 and this study uses version 3), we first downloaded the exact positions of all thalamic neurons. Then, we aligned the thalamic volume to the coordinate system used to build the model and we selected the neurons within the defined volumetric delineation. The volume, number, and type of cells, and resulting densities for each partition of the scaffold are reported in Table 1.

To further confirm the motor-specific targeting of our neuronal placement, we examined the distribution of positioned neurons across serial coronal sections. We confirmed that cells were exclusively placed within motor-related nuclei (VAL, VM, and motor RT) while avoiding non-motor regions such as the ventro-posterior nucleus (VP) (Fig. S5).

Note that, although the BBP Mouse Cell Atlas reports a considerable number of inhibitory interneurons in the VAL and VM, we didn't include them in the model because those are most likely boundary effects in their large-scale cell labeling due to the proximity with the RT nucleus. Thalamic inhibitory interneurons in rodents are mostly localized towards the dorsal sensory nuclei[53], and a two-photon imaging study only reports 4 ± 3 and 4 ± 2 interneurons in the mice VAL and VM, respectively[54]. Thus, we kept all the reported neuron positions regardless of their neuron type, but considered all thalamocortical neurons to be excitatory.

Network connectivity

After establishing the cell positions, we designed connectivity rules to accurately wire the network. Given that thalamocortical relay cells lack reciprocal connections[36], we developed algorithmic strategies to assign the connections from thalamocortical to reticular cells, from reticular cells to other reticular cells, and from reticular cells to thalamocortical cells. Since a precise mapping at the single-cell level of the motor thalamus is currently lacking, we designed the rules combining both data and anatomically-motivated assumptions. The three strategies have a common structure: synaptic candidates are initially selected based on the cells' coordinates through spatial filtering, and connections are then assigned within the candidates set following a divergence ratio that reflects literature data.

Thalamocortical neurons densely innervate the RT nucleus via collateral branches forming from their main axonal trunk en route to the cortex[24,55]. We modeled this organization by assigning a branching point coordinate to each cell with a scalar field. The field was computed to model the parallel trajectories that thalamocortical axons follow before traversing the RT nucleus[41]. This regular organization arises from the early developmental processes governing thalamocortical projections[56]. During early development, thalamocortical axons traverse the internal capsule through a narrow path before reaching the dorsal telencephalon, guided by transcription factors[57] and guidepost cells[58].

To mimic this highly topographic organization, each voxel in VAL and VM nucleus was mapped to a corresponding voxel in RT following geometrical constraints. Specifically, we sliced the meshes corresponding to the union of VAL and VM, and the motor sector of RT, with horizontal slices. We upsampled the corresponding sliced contours to contain an equal number of points and ordered these points according to the first three principal components extracted from the surface points of the RT motor sector. As we ended up with an equal number of points for both shapes with a common ordering, we simply paired the points from source to target based on their index.

Then, we obtained the vector linking each pair of coupled points, and used the identified vectors as linear interpolators to derive a vector field for each voxel within the VAL and VM volumes (as shown in Fig. 2). Each thalamocortical cell was assigned a branching point in the RT nucleus based on the direction of the vector corresponding to the voxel in which its soma lied.

The reticular cells contained within a cylinder oriented as the thickness of the motor reticular sector were selected as synaptic candidates for the thalamocortical cell, using a method based on Plücker coordinates[59]. These coordinates uniquely represent any line in 3D space using two vectors: a direction vector ($\mathbf{l}$) specifying the line's orientation, and a moment vector ($\mathbf{m}$) encoding the line's position relative to the origin of the coordinate system. This six-parameter representation enables the mathematical description of arbitrary 3D volumes by defining their constituent lines, and we used it to identify the axis of the cylinders modeling the spread of axon collaterals from each thalamocortical cell's branching point. An example of the process is visually shown in Fig. 2 inset.

Mathematically, the cylinder axis was represented as a directed line $L = (\mathbf{l}, \mathbf{m})$, where $\mathbf{l} = \mathbf{p}_2 - \mathbf{p}_1$ is the direction vector between end points $\mathbf{p}_1$ and $\mathbf{p}_2$, and $\mathbf{m} = \mathbf{p}_1 \times \mathbf{p}_2$ is the moment vector. The points $\mathbf{p}_1$ and $\mathbf{p}_2$ are the bases of the cylinder, represented as [x,y,z] coordinate vectors.

For a reticular cell at position $\mathbf{p}_{\mathrm{RT\,cell}}$, we computed its perpendicular distance to the cylinder axis d, and the baricentric coordinates of its projection on the cylinder axis with respect to the endpoints, $(\omega_1 : \omega_2)$:

$$\begin{aligned} d &= \frac{|\mathbf{m} + \mathbf{l} \times \mathbf{p}_{\mathrm{RTcell}}|}{|\mathbf{l}|} \\ \mathbf{p}_{\mathrm{proj}} &= \mathbf{p}_{\mathrm{RTcell}} + \frac{\mathbf{l} \times (\mathbf{m} + \mathbf{l} \times \mathbf{p}_{\mathrm{RTcell}})}{|\mathbf{l}|^2} \\ &= \omega_1 * \mathbf{p}_1 + \omega_2 * \mathbf{p}_2, \text{ with } \omega_i = \frac{|\mathbf{p}_{\mathrm{proj}} \times \mathbf{p}_i|}{|\mathbf{m}|} \end{aligned}$$

The reticular cell was selected as synaptic candidate if the perpendicular distance d was lower or equal to the cylinder radius r (thus its distance from the axis was lower than the radius), and if its projection $\mathbf{p}_{\mathrm{proj}}$ fell within the cylinder extremities ($0 \le \omega_i \le 1$). See the inset in Fig. 2.

The cylinder radius was sampled for each thalamocortical cell from a uniform distribution, $r \in \mathcal{U}(90, 190)$. The coefficients of the distribution were chosen according to literature, as collaterals stemming from thalamocortical axons can be divided in two distinct groups: either simple and spatially restricted, or complex and spatially extended. The average maximum collateral length for these two groups is 90 and 190 µm, respectively[41]. The choice of a flat cylindric mask is justified by the spatial organization between reticular dendrites and thalamic axon collaterals: reticular dendrites run approximately parallel to one another and generally lie at perpendicular angles to the axons traversing the nucleus[60]. The axon collaterals, on the other hand, stem from the main axon forming large angles[41], almost in a perpendicular fashion: restricting the point cloud to a cylinder, as opposed to a sphere, avoids to select synaptic candidate that would be targeted by collaterals co-directional to the axon itself.

The number of connections for each thalamocortical cell was picked randomly from a beta distribution, $\mathcal{B}(2.5, 15)$, scaled to have its peak centered around values known from literature. The number of reticular cell bodies within the area covered by collaterals is reported to vary on average between 1 and 44, but the study states that the actual number of cells contacted by collaterals can be larger because of the long dendrites of reticular cells[41,61]. Thus, we centered the peak around the half of the interval, and tuned the beta distribution coefficients to have a longer tail. The coefficients were qualitatively chosen to obtain a profile that was similar to the degree distributions observed in brain networks[62]. The whole connection strategy is depicted in Fig. 2.

Reticular cells form reciprocal dendro-dendritical connections through gap junctions[25,63] in an unstructured manner (i.e., both within a reticular subnetwork and between different reticular subnetworks), providing a substrate to functionally link the activity of thalamic nuclei across different modalities[64]. The synaptic connectivity within the RT nucleus has been extensively studied and is considered to be essential for precise inhibitory control of thalamocortical relay cells[27,65].

Reticular cells have primary dendrites that run parallel to the borders of the RT nucleus, extending for relatively long distances[61]. They form discoidal clusters of connected cells narrowly elongated within the RT plane[27,46], with both chemical GABAergic synapses and bi-directional electrical synapses through gap junctions.

To incorporate this knowledge into our model, synaptic candidates were chosen with an ellipsoidal mask centered around each reticular cell (Fig. 3). Specifically, we selected potential postsynaptic cells based on a general ellipsoid equation. A cell with coordinate [x,y,z] was selected as a synaptic candidate if it satisfied the equation:

$$\left(\frac{x-x_0}{a}\right)^2+\left(\frac{y-y_0}{b}\right)^2+\left(\frac{z-z_0}{c}\right)^2\le 1$$

with a, b, c the ellipsoid semi-axes and $[x_0, y_0, z_0]$ the spatial coordinate of the presynaptic reticular cell.

The ellipsoid was oriented according to the first three principal components extracted from the coordinates of the RT sector vertices. The value of the semiaxes were chosen according to literature: we used the values of spatial influence of chemical and electrical connectivity reported in Deleuze and Huguenard[27]. We extracted the values of the distributions shown in Fig. 8 of the study, and assigned them to the corresponding ellipsoid axes. The length of the electrical maps measured in horizontal and coronal slices in the study corresponds to the ellipsoid axes aligned to the first and second components, respectively. The width of the maps corresponds to the axis parallel to the third component[27]. This yielded values of 180, 95, 42 μm for the semi-axes of ellipsoids used to assign chemical connections and 112, 115, 55 μm for those used for identifying gap junctions.

The number of connections for each reticular cell was sampled within the range observed in experimental data, varying between 2 and 21 neurons per cluster[46], with a beta distribution similarly tuned as the one used to assign the thalamo-reticular connections.

Projections from the RT nucleus to the thalamus exhibit a well-organized topography, where individual reticular neurons predominantly innervate a restricted territory within a single thalamic nucleus in a parallel fashion[66]. Projection patterns are reported to be reciprocal, with reticular neurons projecting back only to the corresponding thalamic nuclei of their sector[47,67]. To replicate this topographic organization, we applied the same scalar field approach used for thalamoreticular connectivity, inverting the direction of scalar field values.

Reticular neuron axons are mostly composed of single arbors with a dense central core, surrounded by sparse components[47]. We modeled the intricate branching of the dense core, growing synthetic branches in confined subvolumes of the VAL-VM nuclei using a space colonization algorithm[28]. More precisely, we first received data from Hádinger et al.[29], obtaining the reconstructed axonal target zone and soma position of 11 reticular cells specifically targeting either VAL or VM. We then registered the data to the CCF volume with an open-source pipeline[39], expanded the flat sections belonging to a single cell into a 3D volume and stored the processed data as axonal boundaries templates (Fig. 4).

Each reticular cell was assigned a template randomly, positioned within the VAL-VM volume according to the element in the vector field corresponding to the RT voxel occupied by the cell itself. A synthetic axonal core was grown inside the positioned volume using the space colonization algorithm. The volumes were first filled with virtual points using a random Gaussian field[68], mimicking the role of axonal guidance cues[69]. Then, a branching structure was iteratively created within the volume to serve as a spatial mask (Fig. 4). Thalamocortical cells located within 43.5 μm from the structure were considered potential synaptic targets. The value was chosen as a quarter of the average dendritic length (174 μm), computed performing a morphometric analysis on VAL-VM thalamocortical cells obtained from the MouseLight portal[70]. This is in accordance with the fact that reticular cells tend to contact proximal regions of thalamocortical dendrites[42].

The number of thalamocortical connections for each reticular cell varied according to the formula:

$$n = d_{\text{boutons}} \cdot l_{\text{arbor}}$$

with $d = 0.124$ boutons μm^{-1}, the density of boutons per axonal length[13] and l_{arbor} the path length of the synthetic axonal core.

Network simulations

To investigate the functional properties of the proposed model, we simulated the full-scale anatomical scaffold with all reconstructed TC and RT neurons using the NEST (v3.8.0, development build compiled May 25 2025). Individual neurons were modeled using the AdEx formalism, selected for its computational efficiency and ability to reproduce essential thalamic firing modes, including tonic spiking and low-threshold rebound bursting[30].

TC neurons were parameterized with subthreshold adaptation a = 40 nS and spike-triggered adaptation b = 5 pA to generate characteristic relay cell responses. RT neurons employed stronger adaptation (a = 80 nS, b = 30 pA) to generate characteristic pacemaker dynamics. All other parameters (membrane capacitance C_m = 200 pF, leak conductance g_L = 10 nS, leak reversal E_L = −60 mV, spike threshold V_{th} = −50 mV) were identical between cell types. Complete parameter specifications are provided in Table S3.

Chemical synapses employed dual-exponential conductances with cell-type-specific kinetics parameters detailed in Table S3, representing fast neurotransmitter-mediated currents. Conduction delays scaled linearly with inter-somatic distance, and were computed for every synaptic connection based on the Euclidean distance r between pre- and post-synaptic somas.

Specifically, the transmission delay $d(r)$ was defined as:

$$d(r) = d_{\text{syn}} + r/c,$$

where d_{syn} represents baseline synaptic latency and c represents axonal conduction velocity.

Baseline synaptic latency was set to 0.2 ms for TC ↔ RT connections, and 0.3 ms for intra-reticular connections. We considered an axonal conduction velocity of 2.0 m s^{-1} for TC and RT axons projecting to the opposite cell type, consistent with thin, unmyelinated or lightly myelinated local fibers[71]. Intra-reticular axons were assigned a slower conduction velocity of 1.0 m s^{-1}, reflecting their short-range connections.

Similarly, synaptic weights were proportionally scaled to represent the effect spatial extension of axonal arborization on connection strengths. Distance-dependent weights $w(r)$ were computed following an exponential decay profile for TC ↔ RT projections ($w(r) = A \cdot e^{-r/\beta}$) and a Gaussian profile for intra-reticular connections ($w(r) = A \cdot e^{-r^2/2\sigma^2}$). All synaptic parameters are reported in Table S3.

Gap junctions between RT neurons, while anatomically present in the scaffold as identified through the reconstruction procedures described above, were not functionally implemented as electrical synapses in our simulations. Instead, all anatomically identified gap junction connections were treated as fast $GABA_A$ chemical synapses. This simplification allowed us to focus the initial analysis on the topological influence of structure on chemical transmission dynamics, given limited anatomical constraints for electrical coupling in motor thalamus.

To ensure that observed dynamics emerged from intrinsic network architecture rather than structured input, self-sustained activity was initiated via a spatially incoherent stimulus. A random subset of TC neurons (20% of the population) received a brief, transient train of Poisson spikes (1000 Hz for 25 ms) via excitatory synapses. After the initialization window (10–35 ms), the external drive was removed, and the network evolved autonomously for a total of 8000 ms simulated.

To test the hypothesis that the scaffold's specific topographic organization and physical scale are necessary for physiological dynamics, we compared the full model against two ablation conditions.

In the first control condition, the distance-dependent component of the weights was removed, testing the functional role of the spatial dispersion of spiking activity caused by the scaffold's physical dimensions. Note that the synaptic amplitude A was downscaled in this condition to avoid network activity saturation.

In the second control condition, the network topology was shuffled while preserving the degree distribution and distance-dependent rules, testing the functional role of the specific anatomical topography reconstructed in the scaffold.

Network activity was analyzed using a population firing rate proxy calculated by convolving spike trains with a Gaussian kernel ($\sigma = 10$ ms). Spindle-band oscillations were isolated using a 7 Hz to 14 Hz bandpass filter. Phase-locking values (PLV) were computed to quantify TC-RT synchronization. Spatial wave propagation velocity was estimated by extracting a spike density field and combining its gradients computed across the spatial and temporal dimensions.

Population firing rate proxy

Population-level activity was estimated by computing an instantaneous firing rate proxy analogous to local field potential recordings. For each population (RT and TC separately), spike trains were convolved with a Gaussian kernel to produce continuous rate estimates:

$$r(t) = \sum_{i=1}^{N} \sum_{k} K(t - t_i^k),$$

where t_i^k denotes the k-th spike time of neuron i, and $K(t)$ is a Gaussian kernel:

$$K(t) = \frac{1}{\sigma\sqrt{2\pi}} \exp(-\frac{t^2}{2\sigma^2})$$

The kernel width was set to $\sigma = 10$ ms, chosen to smooth individual spike events while preserving oscillatory structure at spindle frequencies (~ 10 Hz, period ~ 100 ms). The population-averaged firing rate was obtained by averaging instantaneous rates across all neurons within each population:

$$\mathrm{LFP}_{\mathrm{pop}}(t) = \frac{1}{N} \sum_{i=1}^{N} r_i(t)$$

Signal filtering

To remove low-frequency drift and DC components, the RT population firing rate proxy was high-pass filtered using a third-order Butterworth filter with a cutoff frequency of 2.5 Hz. The filter was applied using zero-phase forward-backward filtering to prevent temporal distortion.

For phase-locking analysis, both RT and TC population signals were bandpass filtered to isolate spindle-band activity. A third-order Butterworth filter with passband 7 Hz to 14 Hz was applied using zero-phase filtering.

Phase synchronization analysis

Phase-locking between TC and RT populations was quantified using the Phase Locking Value (PLV). Instantaneous phases were extracted from spindle-filtered signals using the Hilbert transform:

$$\phi_{\mathrm{TC}}(t) = \arg[\mathcal{H}(\mathrm{LFP}_{\mathrm{TC}}(t))],\ \phi_{\mathrm{RT}}(t) = \arg[\mathcal{H}(\mathrm{LFP}_{\mathrm{RT}}(t))]$$

where $\mathcal{H}$ denotes the Hilbert transform and arg extracts the instantaneous phase. The phase difference was computed as:

$$\Delta\phi(t) = \phi_{TC}(t) - \phi_{RT}(t)$$

The PLV quantifies phase coherence across time:

$$PLV = |\frac{1}{T} \sum_{t=1}^{T} e^{i\Delta\phi(t)}|$$

PLV ranges from 0 (no phase locking) to 1 (perfect phase locking). Values above 0.85 indicate strong temporal coordination.

Four-dimensional spike density field

To analyze spatiotemporal wave propagation, continuous four-dimensional density fields $\rho(x, y, z, t)$ were constructed from discrete spike events. Spike data were organized with columns $[t, x, y, z]$ representing spike times (ms) and three-dimensional neuron positions (μm). The density field was computed in three stages:

1. *Grid construction.*
   Coordinate grids were established with spatial resolution of 25 μm and temporal resolution of 2 ms. Grid bounds were determined from the data range with padding of $2\sigma_{\mathrm{spatial}}$ on spatial dimensions and $2\sigma_{\mathrm{temporal}}$ on the temporal dimension to mitigate boundary artifacts.
2. *Spike histogram.*
   A four-dimensional histogram was constructed by binning spike events into the (t, x, y, z) grid, producing a discrete spike count field $S(i, j, k, l)$ where indices correspond to temporal and spatial bins.
3. *Gaussian smoothing.*
   The spike histogram was convolved with a four-dimensional separable Gaussian kernel to produce the continuous density field:

$$\rho(t, x, y, z) = S(t, x, y, z) * G_{\sigma_t}(t) \otimes G_{\sigma_s}(x) \otimes G_{\sigma_s}(y) \otimes G_{\sigma_s}(z),$$

where G_σ denotes a Gaussian kernel with standard deviation σ, and $\otimes$ represents spatial convolution. Smoothing parameters were $\sigma_{\mathrm{spatial}} = 75\,\mu$m and $\sigma_{\mathrm{temporal}} = 15$ ms. Kernels were truncated at $\pm 3\sigma$ for computational efficiency.

Flow field computation

Local propagation velocity was estimated using the phase gradient method, which assumes that wave propagation follows a conservation equation:

$$\frac{\partial\rho}{\partial t} + \nabla \cdot (\rho \mathbf{v}) = 0$$

Under the assumption of smooth velocity fields, this yields:

$$\mathbf{v} = -\frac{\partial\rho/\partial t}{|\nabla\rho|^2} \nabla\rho$$

Gradients were computed using centered finite differences:

$$\frac{\partial\rho}{\partial t} = \frac{\rho(t + \Delta t) - \rho(t - \Delta t)}{2\Delta t},\ \Delta t = 2\,ms$$

$$\frac{\partial\rho}{\partial x} = \frac{\rho(x + \Delta x) - \rho(x - \Delta x)}{2\Delta x},\ \Delta x = 25\,\mu m$$

with analogous expressions for y and z components. Division by zero was prevented by imposing a floor of $|\nabla\rho|^2 \geq 10^{-10}$.

The instantaneous speed field was computed as:

$$s(t, x, y, z) = |\mathbf{v}| = \sqrt{v_x^2 + v_y^2 + v_z^2}$$

Wavefront velocity extraction

To isolate propagating activity from background noise, an empirical density threshold was applied at each timestamp. At time t, voxels were classified as

part of the active wavefront if their density exceeded the 50th percentile of non-zero density values:

$$W_t = \{(x, y, z) : \rho(t, x, y, z) \geq \text{median}(\rho_t[\rho_t > 0])\}$$

Timestamps with fewer than 100 active voxels were excluded from velocity analysis. For valid timestamps, speeds within the wavefront mask were extracted:

$$S_t = \{s(t, x, y, z) : (x, y, z) \in W_t \; and \; s \; is \; \text{finite and non} - \text{negative}\}$$

Wave propagation characteristics were summarized using the median wave velocity: $v_{\text{wave}} = \text{median}(\bigcup_t S_t)$, providing a robust central estimate insensitive to outliers.

Statistics and reproducibility

Statistical analysis and plotting were performed with Python, while figures were assembled with Adobe Illustrator (v28.3). Pearson correlation coefficients were computed using the "pearsonr" function from the SciPy package (v1.16.3) using default arguments, thus the statistical tests carried out in this study were two-tailed.

To assess the robustness of stochastic connectivity assignment rather than to derive inferential statistics, the scaffold model was instantiated five times with identical parameters ($n = 5$ independent scaffold model instances). Degree distributions were computed across all instances as a sensitivity check, confirming that reported connectivity properties are not artifacts of a single random seed. Topographic validation analyses sampled n = 365 and n = 78 cells, respectively, with sample sizes reported in figure legends. Network simulations were performed on single scaffold instances. Accordingly, the phase-locking value (PLV), wavefront propagation velocities, and ablation condition comparisons are reported as descriptive metrics characterizing individual simulation runs; no inferential statistics or confidence intervals are applicable to these measures. No data were excluded from analyses.

The code and data required to reproduce all analyses are available through Zenodo (https://doi.org/10.5281/zenodo.15198488)[72]. Ethical approval is not required for secondary analysis of public data.

Reporting summary

Further information on research design is available in the Nature Portfolio Reporting Summary linked to this article.

Data availability

The anatomical data used in this study, including publicly available datasets and derived structural information, have been deposited in Zenodo and are openly accessible without restrictions (DOI: 10.5281/zenodo.15198488)[72]. Source data for all figures can be obtained from the same repository. The scaffold model was built using Python 3.10.8 with the BSB v4.2.0. Network simulations were performed using Python 3.11 and NEST v3.8.0 (development build, compiled May 25 2025). Statistical analyses and figure generation were performed using Python 3.11 with NumPy v1.26.3, SciPy v1.16.3, pandas v2.2.1, matplotlib v3.8.2, and seaborn v0.13.2. Figures were assembled using Adobe Illustrator v28.3.

Code availability

The Python code used to build the thalamic model, replicate the manuscript's figures, and process the associated anatomical data is openly accessible without restrictions in Zenodo (https://doi.org/10.5281/zenodo.15198488)[72].

Received: 16 April 2025; Accepted: 30 March 2026;
Published online: 18 April 2026

References

1. Sherman, S. M. Functioning of circuits connecting thalamus and cortex. In *Comprehensive Physiology*, 713–739 (John Wiley & Sons, Ltd, 2017).
2. Shepherd, G. M. G. & Yamawaki, N. Untangling the cortico-thalamo-cortical loop: cellular pieces of a knotty circuit puzzle. *Nat. Rev. Neurosci.* **22**, 389–406 (2021).
3. Shine, J. M., Lewis, L. D., Garrett, D. D. & Hwang, K. The impact of the human thalamus on brain-wide information processing. *Nat. Rev. Neurosci.* **24**, 416–430 (2023).
4. Acsády, L. Organization of thalamic inputs. In Halassa, M. M. (ed.) *The Thalamus*, 27–44 (Cambridge University Press, 2022).
5. Casas-Torremocha, D. et al. A combinatorial input landscape in the "higher-order relay" posterior thalamic nucleus. *J. Neurosci.* **42**, 7757–7781 (2022).
6. Worden, R., Bennett, M. S. & Neacsu, V. The thalamus as a blackboard for perception and planning. *Front. Behav. Neurosci.* **15**, 633872 (2021).
7. Bosch-Bouju, C., Hyland, B. I. & Parr-Brownlie, L. C. Motor thalamus integration of cortical, cerebellar and basal ganglia information: Implications for normal and Parkinsonian conditions. *Front. Comput. Neurosci.***7** (2013).
8. Destexhe, A., Bal, T., McCormick, D. A. & Sejnowski, T. J. Ionic mechanisms underlying synchronized oscillations and propagating waves in a model of ferret thalamic slices. *J. Neurophysiol.* **76**, 2049–2070 (1996).
9. Golomb, D., Wang, X. J. & Rinzel, J. Propagation of spindle waves in a thalamic slice model. *J. Neurophysiol.* **75**, 750–769 (1996).
10. Destexhe, A. Self-sustained asynchronous irregular states and up–down states in thalamic, cortical and thalamocortical networks of nonlinear integrate-and-fire neurons. *J. Comput Neurosci.* **27**, 493–506 (2009).
11. Izhikevich, E. M. & Edelman, G. M. Large-scale model of mammalian thalamocortical systems. *Proc. Natl. Acad. Sci.* **105**, 3593–3598 (2008).
12. Hill, S. & Tononi, G. Modeling sleep and wakefulness in the thalamocortical system. *J. Neurophysiol.* **93**, 1671–1698 (2005).
13. Iavarone, E. et al. Thalamic control of sensory processing and spindles in a biophysical somatosensory thalamoreticular circuit model of wakefulness and sleep. *Cell Rep.* **42**, 112200 (2023).
14. Zheng, W.-L., Wu, Z., Hummos, A., Yang, G. R. & Halassa, M. M. Rapid context inference in a thalamocortical model using recurrent neural networks. *Nat. Commun.***15** (2024). https://doi.org/10.1038/s41467-024-52289-3.
15. Billeh, Y. N. et al. Systematic integration of structural and functional data into multi-scale models of mouse primary visual cortex. *Neuron* **106**, 388–403.e18 (2020).
16. Borges, F. S., Moreira, J. V. S., Takarabe, L. M., Lytton, W. W. & Dura-Bernal, S. Large-scale biophysically detailed model of somatosensory thalamocortical circuits in NetPyNE. *Front. Neuroinform.* **16**, 884245 (2022).
17. Barardi, A., Garcia-Ojalvo, J. & Mazzoni, A. Transition between functional regimes in an integrate-and-fire network model of the thalamus. *PLOS ONE* **11**, e0161934 (2016).
18. Barabási, D. L. et al. Neuroscience needs network science. *J. Neurosci.* **43**, 5989–5995 (2023).
19. Phillips, J. W. et al. A repeated molecular architecture across thalamic pathways. *Nat. Neurosci.* **22**, 1925–1935 (2019).
20. Alonso-Martínez, C., Rubio-Teves, M., Casas-Torremocha, D., Porrero, C. & Clascá, F. Cerebellar and basal ganglia inputs define three main nuclei in the mouse ventral motor thalamus. *Front. Neuroanat.* **17**, 1242839 (2023).

21. De Schepper, R. et al. Model simulations unveil the structure-function-dynamics relationship of the cerebellar cortical microcircuit. *Commun. Biol.* **5**, 1240 (2022).
22. Wang, Q. et al. The allen mouse brain common coordinate framework: A 3D reference atlas. *Cell* **181**, 936–953.e20 (2020).
23. Katz, D. & Chandar, K. Thalamus. In *Encyclopedia of the Neurological Sciences*, 425–430 (Elsevier, 2014).
24. Pinault, D. The thalamic reticular nucleus: structure, function and concept. *Brain Res. Brain Res. Rev.* **46**, 1–31 (2004).
25. Crabtree, J. W. Functional diversity of thalamic reticular subnetworks. *Front. Syst. Neurosci.* **12**, 41 (2018).
26. Erö, C., Gewaltig, M.-O., Keller, D. & Markram, H. A cell atlas for the mouse brain. *Front. Neuroinform.* **12**, 84 (2018).
27. Deleuze, C. & Huguenard, J. R. Distinct electrical and chemical connectivity maps in the thalamic reticular nucleus: potential roles in synchronization and sensation. *J. Neurosci.* **26**, 8633–8645 (2006).
28. Runions, A., Lane, B. & Prusinkiewicz, P. Modeling trees with a space colonization algorithm. In *Proc. Eurographics Workshop on Natural Phenomena*, 63–70 (2007).
29. Hádinger, N. et al. Region-selective control of the thalamic reticular nucleus via cortical layer 5 pyramidal cells. *Nat. Neurosci.* **26**, 116–130 (2023).
30. Brette, R. & Gerstner, W. Adaptive exponential integrate-and-fire model as an effective description of neuronal activity. *J. Neurophysiol.* **94**, 3637–3642 (2005).
31. Li, Y. et al. Distinct subnetworks of the thalamic reticular nucleus. *Nature* **583**, 819–824 (2020).
32. Lam, Y.-W. & Sherman, S. M. Functional organization of the thalamic input to the thalamic reticular nucleus. *J. Neurosci.* **31**, 6791–6799 (2011).
33. Lam, Y.-W. & Sherman, S. M. Functional topographic organization of the motor reticulothalamic pathway. *J. Neurophysiol.* **113**, 3090–3097 (2015).
34. Binas, J., Rutishauser, U., Indiveri, G. & Pfeiffer, M. Learning and stabilization of winner-take-all dynamics through interacting excitatory and inhibitory plasticity. *Front. Comput. Neurosci.* **8** (2014).
35. Halassa, M. M. & Acsády, L. Thalamic inhibition: diverse sources, diverse scales. *Trends Neurosci.* **39**, 680–693 (2016).
36. O'Reilly, C., Iavarone, E., Yi, J. & Hill, S. L. Rodent somatosensory thalamocortical circuitry: neurons, synapses, and connectivity. *Neurosci. Biobehav. Rev.* **126**, 213–235 (2021).
37. Dice, L. R. Measures of the amount of ecologic association between species. *Ecology* **26**, 297–302 (1945).
38. Zou, K. H. et al. Statistical validation of image segmentation quality based on a spatial overlap index. *Acad. Radiol.* **11**, 178–189 (2004).
39. Timonidis, N. et al. Analyzing thalamocortical tract-tracing experiments in a common reference space. *Neuroinformatics* **22**, 103–122 (2023).
40. Gupta, A. K. & Nadarajah, S. (eds.) *Handbook of Beta Distribution and Its Applications* (CRC Press, 2004).
41. Harris, R. M. Axon collaterals in the thalamic reticular nucleus from thalamocortical neurons of the rat ventrobasal thalamus. *J. Comp. Neurol.* **258**, 397–406 (1987).
42. Campbell, P. W., Govindaiah, G., Masterson, S. P., Bickford, M. E. & Guido, W. Synaptic properties of the feedback connections from the thalamic reticular nucleus to the dorsal lateral geniculate nucleus. *J. Neurophysiol.* **124**, 404–417 (2020).
43. Destexhe, A. & Sejnowski, T. J. Interactions between membrane conductances underlying thalamocortical slow-wave oscillations. *Physiol. Rev.* **83**, 1401–1453 (2003).
44. Destexhe, A., Contreras, D., Sejnowski, T. J. & Steriade, M. A model of spindle rhythmicity in the isolated thalamic reticular nucleus. *J. Neurophysiol.* **72**, 803–818 (1994).
45. Gambosi, B. et al. A model with dopamine depletion in basal ganglia and cerebellum predicts changes in thalamocortical beta oscillations. *Int. J. Neural Syst.* **34**, 2450045 (2024).
46. Lee, S.-C., Patrick, S. L., Richardson, K. A. & Connors, B. W. Two functionally distinct networks of gap junction-coupled inhibitory neurons in the thalamic reticular nucleus. *J. Neurosci.* **34**, 13170–13182 (2014).
47. Pinault, D. & Deschênes, M. Projection and innervation patterns of individual thalamic reticular axons in the thalamus of the adult rat: a three-dimensional, graphic, and morphometric analysis. *J. Comp. Neurol.* **391**, 180–203 (1998).
48. Lein, E. S. et al. Genome-wide atlas of gene expression in the adult mouse brain. *Nature* **445**, 168–176 (2007).
49. Hyman, J. M. Accurate monotonicity preserving cubic interpolation. *SIAM J. Sci. Stat. Comput.* **4**, 645–654 (1983).
50. Dan E. L., Di^nşoreanu M., Mureşan R. C. Accuracy of six interpolation methods applied on pupil diameter data. In *Proc. IEEE International Conference on Automation, Quality and Testing, Robotics (AQTR)*, 1–5 (2020).
51. Jaffar, A. et al. Spatial interpolation method comparison for physico-chemical parameters of river water in Klang River using MATLAB. *Bull. Electr. Eng. Inform.* **11**, 2368–2377 (2022).
52. Oh, S. W. et al. A mesoscale connectome of the mouse brain. *Nature* **508**, 207–214 (2014).
53. Huerga-Gómez, I., Martini, F. J. & López-Bendito, G. Building thalamic neuronal networks during mouse development. *Front. Neural Circuits* **17**, 1131424 (2023).
54. Jager, P. et al. Dual midbrain and forebrain origins of thalamic inhibitory interneurons. *eLife* **10**, e59272 (2021).
55. Jones, E. G. Some aspects of the organization of the thalamic reticular complex. *J. Comp. Neurol.* **162**, 285–308 (1975).
56. Vanderhaeghen, P. & Polleux, F. Developmental mechanisms patterning thalamocortical projections: Intrinsic, extrinsic and in between. *Trends Neurosci.* **27**, 384–391 (2004).
57. Molnár, Z. & Kwan, K. Y. Development and evolution of thalamocortical connectivity. *Cold Spring Harb. Perspect. Biol.* **16**, a041503 (2024).
58. Garel, S., Yun, K., Grosschedl, R. & Rubenstein, J. L. R. The early topography of thalamocortical projections is shifted in Ebf1 and Dlx1/2 mutant mice. *Development* **129**, 5621–5634 (2002).
59. Stolfi, J. *Primitives for Computational Geometry*. Ph.D. thesis (Stanford University, 1988).
60. Ohara, P. T. & Lieberman, A. R. The thalamic reticular nucleus of the adult rat: experimental anatomical studies. *J. Neurocytol.* **14**, 365–411 (1985).
61. Lübke, J. Morphology of neurons in the thalamic reticular nucleus (TRN) of mammals as revealed by intracellular injections into fixed brain slices. *J. Comp. Neurol.* **329**, 458–471 (1993).
62. Giacopelli, G., Tegolo, D., Spera, E. & Migliore, M. On the structural connectivity of large-scale models of brain networks at cellular level. *Sci. Rep.* **11**, 4345 (2021).
63. Pinault, D. The thalamic reticular nucleus: anatomo-functional mechanisms and concept. In Usrey, W. M., Sherman, S. M. (eds.) *The Cerebral Cortex and Thalamus*, 1 edn. 163–176 (Oxford University Press, 2023).
64. Vaughn, M. J., Laswick, Z., Wang, H., Haas, J. S. Functionally distinct circuits are linked by heterocellular electrical synapses in the thalamic reticular nucleus. *eNeuro* **11** (2024).
65. Long, M. A., Landisman, C. E. & Connors, B. W. Small clusters of electrically coupled neurons generate synchronous rhythms in the thalamic reticular nucleus. *J. Neurosci.* **24**, 341–349 (2004).
66. Takata, N. Thalamic reticular nucleus in the thalamocortical loop. *Neurosci. Res.* **156**, 32–40 (2020).
67. Cicirata, F., Angaut, P., Serapide, M. F. & Panto, M. R. Functional organization of the direct and indirect projection via the reticularis

thalami nuclear complex from the motor cortex to the thalamic nucleus ventralis lateralis. *Exp. Brain Res.* **79**, 325–337 (1990).
68. Clifford, P. Monte Carlo methods. In *Methods in Experimental Physics*, vol. 28, 125–153 (Elsevier, 1994).
69. Chilton, J. K. Molecular mechanisms of axon guidance. *Dev. Biol.* **292**, 13–24 (2006).
70. Winnubst, J. et al. Reconstruction of 1,000 projection neurons reveals new cell types and organization of long-range connectivity in the mouse brain. *Cell* **179**, 268–281.e13 (2019).
71. Salami, M., Itami, C., Tsumoto, T. & Kimura, F. Change of conduction velocity by regional myelination yields constant latency irrespective of distance between thalamus and cortex. *Proc. Natl. Acad. Sci.* **100**, 6174–6179 (2003).
72. Sheiban, F. J. A Data-driven anatomical model for investigating motor thalamic circuitry (2025). https://doi.org/10.5281/zenodo.15198487.
73. Allen Institute for Brain Science. Allen Mouse Brain Connectivity Atlas. https://connectivity.brain-map.org (2011).
74. Allen Institute for Brain Science. Allen Mouse Brain Atlas. Dataset. https://mouse.brain-map.org (2004).

Acknowledgements

We are grateful to Nóra Hádinger and László Acsády for kindly providing their data in response to our request. We also extend our sincere thanks to Christoph Pokorny, Daniela Egas Santander, Jason P. Smith, and Michael Reimann for their valuable insights and discussions on circuit topology and network validation. F.J.S. is a Ph.D. student enrolled in the National PhD in Artificial Intelligence, XXXVII cycle, course on Health and Life Sciences, organized by Università Campus Bio-Medico di Roma. The work of A.A., A.P., and E.D. is further supported by the Horizon Europe Programme for Research and Innovation under Grant Agreement No. 101147319 (EBRAINS 2.0). This work was funded by the project "EBRAINS-Italy (European Brain ReseArch INfrastructureS-Italy)," granted by the Italian National Recovery and Resilience Plan (NRRP), M4C2, funded by the European Union - NextGenerationEU (Project IR0000011, CUP B51E22000150006, "EBRAINS-Italy") to A.A., A.P., and E.D.; this grant also fully covered the publication fees of this article.

Author contributions

F.J.S. conceived the study, designed and implemented the computational model, performed analyses, created visualizations, and wrote the manuscript. A.A. supervised the study and revised the manuscript. M.F.B. implemented and performed simulations. R.D.S. contributed to BSB implementation. C.A.-M. and M.R.-T. provided anatomical data and contributed to their analysis. F.C. contributed neuroanatomical interpretation and revised the manuscript. E.D. contributed to the study design. A.P. contributed to the study design and supervised its execution, acquired funding, and revised the manuscript.

Competing interests

A.P. is co-founder of Agade Srl and AllyArm Srl; has conducted seminars for Novartis, Pfizer, TEHA, and Accmed; and has received research funding from international bodies (EU FP7, Horizon/HE, NIH, ESA), national public institutions (MIUR PRIN, INAIL, Lombardy Region, ASI), private foundations (Fondazione Cariplo, Fondazione Telethon, Fondazione Valduce, Fondazione FORST), and companies (Kayser Italia Srl, Generali Wellion, Tecnobody Srl, EMAC Srl, Merz Therapeutics, AllyArm Srl). The remaining authors declare no competing interests. The authors confirm that none of the above relationships influenced the design, conduct, or reporting of the present study.

Additional information

Supplementary information The online version contains supplementary material available at https://doi.org/10.1038/s42003-026-10032-2.

Correspondence and requests for materials should be addressed to Francesco Jamal Sheiban.

Peer review information *Communications Biology* thanks Mihail Bota, Hansem Sohn, and the other, anonymous, reviewer for their contribution to the peer review of this work. Primary Handling Editor: Benjamin Bessieres. A peer review file is available.